

# Mixed Convection and Heat Transfer Studies in Non-Uniformly Heated Buoyancy Driven Cavity Flow

A. D. Abin Rejeesh<sup>1</sup>, Selvarasu Udhayakumar<sup>1</sup>, T. V. S. Sekhar<sup>2</sup>, Rajagopalan Sivakumar<sup>1\*</sup>

<sup>1</sup>Department of Physics, Pondicherry University, Puducherry, India

<sup>2</sup>School of Basic Sciences, Indian Institute of Technology Bhubaneswar, Bhubaneswar, India

Email: \*rs4670@gmail.com, \*rsk.phy@pondiuni.edu.in, sekhartvs@iitbbs.ac.in

**How to cite this paper:** Rejeesh, A.D.A., Udhayakumar, S., Sekhar, T.V.S. and Sivakumar, R. (2017) Mixed Convection and Heat Transfer Studies in Non-Uniformly Heated Buoyancy Driven Cavity Flow. *Open Journal of Fluid Dynamics*, 7, 231-262. <https://doi.org/10.4236/ojfd.2017.72016>

**Received:** May 3, 2017

**Accepted:** June 20, 2017

**Published:** June 23, 2017

Copyright © 2017 by authors and Scientific Research Publishing Inc.

This work is licensed under the Creative Commons Attribution-NonCommercial International License (CC BY-NC 4.0).

<http://creativecommons.org/licenses/by-nc/4.0/>



Open Access

## Abstract

We analyse the mixed convection flow in a cavity flow which is driven by buoyancy generated due to a non-uniformly heated top wall which is moving uniformly. A fourth order accurate finite difference scheme is used in this study and our code is first validated against available data in the literature. The results are obtained for different sets of Reynolds number  $Re$ , Prandtl number  $Pr$  and Grashof number  $Gr$  which are in the ranges 100 - 3000, 0.0152 - 10 and  $10^2$  -  $10^6$  respectively. Here  $Gr$  is related to the Richardson number according to  $Ri = Gr/Re^2$ . While increasing the Richardson number, the growth of upstream secondary eddy (USE) is observed together with a degradation of downstream secondary eddy (DSE). When mixed convection is dominant, the upstream secondary eddy and the downstream secondary eddy merge to form a large recirculation region. When the effect of  $Pr$  is studied in the forced convection regime,  $Ri \ll 1$ , the temperature in the central region of the cavity remains nearly a constant. However, in the mixed convection regime, the temperature in cavity undergoes non-monotonic changes. Finally, using the method of divided differences, it is shown that numerical accuracy of the derived numerical scheme used in this work is four.

## Keywords

Navier-Stokes Equation, High Order Compact Scheme, Mixed Convection, Divided Difference Principle

## 1. Introduction

In order to fill the gap between the results of numerical simulations and experiments, several factors have to be considered and one among them is the accuracy and reliability of numerical scheme employed in the simulations. If we use the

traditional second order accurate central difference method, they suffer from computational instability and may not converge when convective terms dominate. While the upwind method suppresses the unwanted physical oscillations and enables us to get solutions for a large range of cell Reynolds numbers, the major disadvantage associated with the upwind method is that its order of accuracy is very low, which is  $\mathcal{O}(h)$  where  $h$  is the grid size. In the past, in order to get optimal solution for the wide range of parameters, researchers generate benchmark results by applying the central difference operator to diffusion terms and upwind to convection dominated part of the governing equation [1]. Recently higher order finite difference schemes have gained importance due to their interesting properties such as unconditional stability, computational cost, effectiveness and hence efficiency in solving non-linear problems.

The study of recirculation of the fluid inside a square cavity forms the basis to many applications including energy engineering, nuclear reactor [2], cooling of electronic devices [3] [4] [5], the study of chaotic mixing [6], production of plane glass, study of coupling between evaporation and condensation [7], and in understanding dynamics of water in lakes and ponds [8]. In particular, if the viscosity of the fluid is strongly temperature dependent, then buoyancy effects mix with the inertial effects, leading to complex flow dynamics. In the fluid flow, if the natural buoyancy driven effect and forced shear driven convection effect have comparable magnitude, we have the mixed convective heat transfer. Experimental results on the mixed convection in the bottom-heated rectangular cavity flow show that the heat transfer coefficient is insensitive to the Richardson number [9]. Experimental studies on the natural convection in tilted rectangular cavity have been studied [10] and it is found that the heat transfer depends on the angle of heating the top wall. It is found that for  $Ri = 10$  multi-cellular flow is observed which alter the isotherm structure. The instability in the mixed convective flow and heat transfer in a cavity for positive and negative values of Grashof number  $Gr$  in which top upper wall is heated with constant temperature are studied [11] and it is found that if the aspect ratio of the cavity is equal to 2, a Hopf bifurcation takes place. A numerical study on the mixed convection lid driven flow in a square cavity with cold vertical walls and sinusoidally heated bottom wall show that the strength of circulation increases with  $Gr$  and irrespective of  $Re$  and  $Pr$  and further that the overall power law correlation for mean  $Nu$  could not be obtained [12]. The effect of different orientation of temperature gradient in the mixed convective heat transfer is studied recently [13] using a finite difference scheme similar to the one in [14] and found that heat transfer rate increases with the decrease of  $Ri$  which is independent of the orientation of temperature gradient on the adiabatic walls. It is also found that a thermally stratified fluid will result when the top wall is heated and bottom wall is kept cold. A further extension of studies to evaluate the effect of Richardson and Prandtl number is also reported [15]. Essentially, most of the studies in the literature focus on the flow and heat transfer properties due to bottom uniformly and non-uniformly heated surfaces [13] [15]-[25], studies emerging due to

heating of vertical walls [26]-[33], reports on uniformly heated top wall [34] [35], and studies employing internal heat sources [36] [37]. A summary of previous studies employing different numerical schemes with various heating configurations is listed in **Table 1**. In the present work, we undertake a systematic analysis of mixed convection flow and associated heat transfer effects in a flow induced by a non-uniformly heated top lid which is moving uniformly using a high order accurate numerical scheme coupled with multigrid method.

**Table 1.** An overview of previous reports on the lid-driven cavity flows with various types of heating configuration and numerical methods used.

<i>Authors</i>	<i>Heat transfer studies</i>	<i>Adiabatic walls</i>	<i>Heating configuration</i>	<i>Numerical method</i>
Ahmed <i>et al.</i> (2016)	MC	Horizontal	Constant heating of bottom corner	FVM
Malleswaran and Sivasankaran (2016)	MC	Horizontal	Constant heating of bottom corner	FVM
Mamourian <i>et al.</i> (2016)	MC	Horizontal	Constant heating of left wall	FVM
Kareem <i>et al.</i> (2016)	MC	Horizontal	Constant heating of bottom wall	FVM
Bettaibi <i>et al.</i> (2015)	MC	None	Varying temperature on bottom wall	LBM
Garooosi <i>et al.</i> (2015)	NC and MC	All walls	Constant heating on square pillars	FVM
Nayak <i>et al.</i> (2015)	MC	Horizontal	Constant heating of left wall	FVM
Kefayati (2015)	MC	Horizontal	Constant heating of left wall	LBM
Kefayati (2014)	MC	Horizontal	Varying temperature on right wall	LBM
Jamai <i>et al.</i> (2014)	NC	Horizontal	Varying temperature on vertical walls	FEM
Karimipour <i>et al.</i> (2014)	MC	Vertical	Constant heating of top wall	LBM
Hussein and Ali (2014)	MC	Vertical	Varying temperature on bottom wall	FDM
Ismael <i>et al.</i> (2014)	MC	Vertical	Constant heating of bottom wall	FDM
Mahapatra <i>et al.</i> (2013)	NC	Horizontal	Varying temperature on left and bottom walls	FDM
Mekroussi <i>et al.</i> (2013)	MC	Vertical	Constant heating on bottom wall	FVM
Al-Salem <i>et al.</i> (2012)	MC	Vertical	Varying temperature on bottom wall	FVM
Kefayati <i>et al.</i> (2012)	MC	Horizontal	Varying temperature on left wall	LBM
Arani <i>et al.</i> (2012)	MC	Horizontal	Varying temperature on vertical walls	FVM
Chamkha and Abu-Nada (2012)	MC	Vertical	Constant heating of top wall	FVM
Basak <i>et al.</i> (2011)	MC	Horizontal	Varying temperature on vertical and bottom walls	FEM
Billah <i>et al.</i> (2011)	MC	Horizontal	Constant heating of rod at the centre	FEM
Cheng (2011)	MC	Vertical	Constant heating on bottom wall	FDM
Nasrin (2011)	MC	Horizontal	Constant heating on right wall	FEM
Cheng and Liu (2010)	MC	Vertical	Constant heating on bottom wall	FDM

**Abbreviation:** MC: Mixed Convection; NC: Natural Convection; LBM: Lattice Boltzmann Method; FVM: Finite Volume Method; FEM: FiniteElement Method; FDM: Finite Difference Method.

## 2. Modelling and Governing Equations

We consider steady, viscous, incompressible fluid which is completely filled inside a square cavity. The schematic diagram for the flow configuration and the boundary condition applied are depicted in **Figure 1**. Only the upper lid is allowed to move with a uniform velocity from left to right. The side vertical walls marked with  $A$  are thermally adiabatic. The Boussinesq approximation for the fluid is applied so that its density variation together with physical movement of lid leads to non-isothermal laminar mixed convection in cavity. The governing equations are Navier-Stokes equations with buoyancy term coupled with energy equation together with incompressibility condition and are given by

$$(\mathbf{q} \cdot \nabla)\mathbf{q} = -\frac{1}{\rho}\nabla p + \nu\nabla^2\mathbf{q} + g\beta(T_h - T_c)\hat{\mathbf{a}}_y \tag{1}$$

$$(\mathbf{q} \cdot \nabla)T = \nabla \cdot (\alpha\nabla T) \tag{2}$$

$$\nabla \cdot \mathbf{q} = 0 \tag{3}$$

where  $\mathbf{q}, p, T$  are velocity, pressure and temperature of the fluid respectively. The kinematic viscosity of the fluid is  $\nu$  and let  $\beta$  be the volumetric coefficient of thermal expansion of the fluid. Let  $T_h$  and  $T_c$  denote the hot and cold wall temperatures and  $\alpha$  be the thermal diffusivity of the fluid. Non-dimensionalization is carried out with the following definitions

$$\mathbf{x} = \frac{\mathbf{x}^*}{H}, \quad \mathbf{y} = \frac{\mathbf{y}^*}{H}, \quad \mathbf{u} = \frac{\mathbf{u}^*}{q_0}, \quad \mathbf{v} = \frac{\mathbf{v}^*}{q_0}, \quad p = \frac{p^*}{\rho q_0^2}, \quad T = \frac{T^* - T_c}{T_h - T_c} \tag{4}$$

where  $*$  denotes physical quantities in dimensional form. Further let the uniform velocity of the top wall be  $q_0 = (u, v) = (1, 0)$ . Based on the above scaling parameters, the non-dimensionalized form of the governing equations are

$$(\mathbf{q} \cdot \nabla)\mathbf{q} = -\nabla p + \frac{1}{Re}\nabla^2\mathbf{q} + \frac{Gr}{Re^2}T\hat{\mathbf{a}}_y \tag{5}$$

$$(\mathbf{q} \cdot \nabla)T = \frac{1}{RePr}\nabla^2T \tag{6}$$

$$\nabla \cdot \mathbf{q} = 0 \tag{7}$$

where  $\hat{\mathbf{a}}_y$  is the unit vector in direction normal to gravitational force and  $T$  denotes the dimensionless temperature of the fluid. The dimensionless parameters for the problem are the Reynolds number  $Re$ , the Grashof number  $Gr$  and the Prandtl number  $Pr$  and a non-independent parameter Richardson

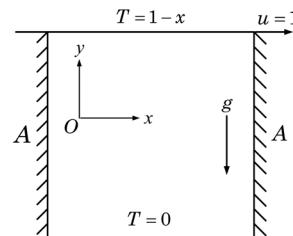


**Figure 1.** Schematic diagram of square cavity with vertical adiabatic walls for mixed convective heat transfer simulation.

number  $Ri$ . In the stream function-vorticity or  $\psi$ - $\omega$  formulation, the governing equations become

$$\frac{\partial^2 \psi}{\partial x^2} + \frac{\partial^2 \psi}{\partial y^2} = -\omega \quad (8)$$

$$u \frac{\partial \omega}{\partial x} + v \frac{\partial \omega}{\partial y} = \frac{1}{Re} \left( \frac{\partial^2 \omega}{\partial x^2} + \frac{\partial^2 \omega}{\partial y^2} \right) + Ri \frac{\partial T}{\partial x} \quad (9)$$

$$u \frac{\partial T}{\partial x} + v \frac{\partial T}{\partial y} = \frac{1}{RePr} \left( \frac{\partial^2 T}{\partial x^2} + \frac{\partial^2 T}{\partial y^2} \right) \quad (10)$$

where  $\omega$  is vorticity of the fluid,  $u$  and  $v$  are defined in terms of streamfunction as

$$\boldsymbol{\omega} = \nabla \times \boldsymbol{q} \quad (11)$$

$$u = \frac{\partial \psi}{\partial y} \quad (12)$$

$$v = -\frac{\partial \psi}{\partial x} \quad (13)$$

The boundary conditions used in the present case are as follows. Let the horizontal and vertical components of velocity  $\boldsymbol{q}$  be  $u$  and  $v$  respectively. Only for the top horizontal wall,  $u=1$  and  $v=0$  is applied. For all other walls,  $u=v=0$ . Also,  $\psi=0$  on all walls. The viscosity of the fluid which is in contact with the surface of the wall generates vorticity  $\omega$  in the fluid, which is given by  $\omega = -\partial^2 \psi / \partial n^2$  where  $n$  refers to a direction perpendicular to the wall. The boundary conditions for temperature is as follows. A linearly varying temperature given by  $T=1-x$  is prescribed for the top moving wall while the bottom horizontal wall is held at fixed temperature given by  $T=0$ . The two vertical walls are held thermodynamically adiabatic which means no heat flux can enter or leave the wall and therefore we have  $\partial T / \partial n = 0$  on the vertical walls. Here  $\boldsymbol{n}$  refers to a direction normal to the surface of the wall.

### 3. Discretization Scheme

Here, we describe the discretization procedure for to the governing set of partial differential equations. Let  $h$  and  $k$  denotes the grid spacing ( $h \neq k$ ) then, from Taylor series expansion, we have, the fourth order accurate finite difference representation for the first and second derivatives as follows.

$$\frac{\partial \phi}{\partial \xi} = D_{\xi} \phi - \frac{h^2}{6} \frac{\partial^3 \phi}{\partial \xi^3} + \mathcal{O}(h^4) \quad (14)$$

$$\frac{\partial^2 \phi}{\partial \xi^2} = D_{\xi}^2 \phi - \frac{h^2}{12} \frac{\partial^4 \phi}{\partial \xi^4} + \mathcal{O}(h^4) \quad (15)$$

$$\frac{\partial \phi}{\partial \eta} = D_{\eta} \phi - \frac{k^2}{6} \frac{\partial^3 \phi}{\partial \eta^3} + \mathcal{O}(h^4) \quad (16)$$

$$\frac{\partial^2 \phi}{\partial \eta^2} = D_{\eta}^2 \phi - \frac{h^2}{12} \frac{\partial^4 \phi}{\partial \eta^4} + \mathcal{O}(h^4) \quad (17)$$

where  $D_\xi$ ,  $D_\xi^2$ ,  $D_\eta$  and  $D_\eta^2$  are second order central difference operators which are given by

$$D_\xi \phi_{i,j} = \frac{\phi_{i+1,j} - \phi_{i-1,j}}{2h} \tag{18}$$

$$D_\xi^2 \phi_{i,j} = \frac{\phi_{i+1,j} - 2\phi_{i,j} + \phi_{i-1,j}}{h^2} \tag{19}$$

$$D_\eta \phi_{i,j} = \frac{\phi_{i,j+1} - \phi_{i,j-1}}{2k} \tag{20}$$

$$D_\eta^2 \phi_{i,j} = \frac{\phi_{i,j+1} - 2\phi_{i,j} + \phi_{i,j-1}}{k^2} \tag{21}$$

Similarly, the higher order cross derivative operators can be written as

$$D_x D_y \phi_{i,j} = \frac{1}{4hk} [\phi_{i+1,j+1} - \phi_{i+1,j-1} - \phi_{i-1,j+1} + \phi_{i-1,j-1}] \tag{22}$$

$$D_x^2 D_y \phi_{i,j} = \frac{1}{2h^2 k} [(\phi_{i+1,j+1} - \phi_{i+1,j-1} + \phi_{i-1,j+1} - \phi_{i-1,j-1}) - 2(\phi_{i,j+1} - \phi_{i,j-1})] \tag{23}$$

$$D_x D_y^2 \phi_{i,j} = \frac{1}{2h k^2} [(\phi_{i+1,j+1} + \phi_{i+1,j-1} - \phi_{i-1,j+1} - \phi_{i-1,j-1}) - 2(\phi_{i+1,j} - \phi_{i-1,j})] \tag{24}$$

$$D_x^2 D_y^2 \phi_{i,j} = \frac{1}{h^2 k^2} [(\phi_{i+1,j+1} + \phi_{i+1,j-1} + \phi_{i-1,j+1} + \phi_{i-1,j-1}) - 2(\phi_{i+1,j} + \phi_{i-1,j} + \phi_{i,j+1} + \phi_{i,j-1}) + 4\phi_{i,j}] \tag{25}$$

### 3.1. Discretization of Streamfunction Equation

Substituting (15) and (17) in the streamfunction Equation (8) and using the  $D$ -operator from Equations (18) to (25) we get finite difference representation of streamfunction equation as given below

$$-D_x^2 \psi_{i,j} - D_y^2 \psi_{i,j} + \omega_{i,j} - \tau_{i,j} = 0 \tag{26}$$

with the truncation error  $\tau_{i,j}$  in the above equation is given by

$$\tau_{i,j} = -\left(\frac{h^2}{12} \frac{\partial^4 \psi}{\partial x^4} + \frac{k^2}{12} \frac{\partial^4 \psi}{\partial y^4}\right)_{i,j} + \mathcal{O}(h^4, k^4) \tag{27}$$

Now, to eliminate higher derivatives of  $\psi$  in the truncation error term, we differentiate Equation (8) once and twice with respect to  $x$  and  $y$  respectively to yield the following.

$$\frac{\partial^3 \psi}{\partial x^3} = -\frac{\partial^3 \psi}{\partial x \partial y^2} - \frac{\partial \omega}{\partial x} \tag{28}$$

$$\frac{\partial^4 \psi}{\partial x^4} = -\frac{\partial^4 \psi}{\partial x^2 \partial y^2} - \frac{\partial^2 \omega}{\partial x^2} \tag{29}$$

$$\frac{\partial^3 \psi}{\partial y^3} = -\frac{\partial^3 \psi}{\partial x^2 \partial y} - \frac{\partial \omega}{\partial y} \tag{30}$$

$$\frac{\partial^4 \psi}{\partial y^4} = -\frac{\partial^4 \psi}{\partial x^2 \partial y^2} - \frac{\partial^2 \omega}{\partial y^2} \tag{31}$$

First we substitute (29) and (31) in (27) and then all the derivatives are replaced by suitable expressions from the set of Equations (18) to (25). The resulting simplified expression for  $\tau_{i,j}$  is substituted in (26) and rearranged so that we obtain the fourth order accurate discretized form of streamfunction Equation (8) as given below.

$$\begin{aligned} &\psi_0(-4d_3 + 2h^2k^2) + \sum_{i=1,3} \psi_i(2d_3 - k^2) + \sum_{i=2,4} \psi_i(2d_3 - h^2) \\ &+ \sum_{i=5}^8 \psi_i(-4d_3 + 2h^2k^2) = -h^2k^2(\omega_0 + d_1D_x^2\omega + d_2D_y^2\omega) \end{aligned} \tag{32}$$

where the constants in the above equations are

$$d_1 = \frac{h^2}{12} \tag{33}$$

$$d_2 = \frac{k^2}{12} \tag{34}$$

$$d_3 = d_1 + d_2 \tag{35}$$

and  $\sum_{i=0}^8 \psi_i$  represents the 8 nearest neighboring points together with a center point on the computational domain.

### 3.2. Discretization of Vorticity Equation

Now, the vorticity Equation (9) is rewritten as

$$\frac{\partial^2 \omega}{\partial x^2} + \frac{\partial^2 \omega}{\partial y^2} + c \frac{\partial \omega}{\partial x} + d \frac{\partial \omega}{\partial y} + q = 0 \tag{36}$$

and the associated coefficients are

$$c = Re \cdot \frac{\partial \psi}{\partial y} \tag{37}$$

$$d = -Re \cdot \frac{\partial \psi}{\partial x} \tag{38}$$

$$q = -Re \cdot Ri \cdot \frac{\partial T}{\partial x} \tag{39}$$

Next, the Equation (36) is written in terms of finite difference operator notation and which is valid for the grid point  $(i, j)$ . Accordingly, the coefficients  $c$ ,  $d$  and  $q$  will have the suffix of the grid point under consideration as given below.

$$-D_x^2 \omega_{i,j} - D_y^2 \omega_{i,j} + c_{i,j} D_x \omega_{i,j} + d_{i,j} D_y \omega_{i,j} + q_{i,j} - \zeta_{i,j} = 0 \tag{40}$$

with a truncation error  $\zeta_{i,j}$  given by

$$\zeta_{i,j} = - \left[ \frac{h^2}{12} \left( \frac{\partial^4 \omega}{\partial x^4} - 2c \frac{\partial^3 \omega}{\partial x^3} \right) + \frac{k^2}{12} \left( \frac{\partial^4 \omega}{\partial y^4} - 2d \frac{\partial^3 \omega}{\partial y^3} \right) \right]_{i,j} + \mathcal{O}(h^4, k^4) \tag{41}$$

To eliminate the derivatives appearing in the truncation error term (41), we differentiate the vorticity Equation (36) to yield the following set of expressions

$$\frac{\partial^3 \omega}{\partial x^3} = - \frac{\partial^3 \omega}{\partial x \partial y^2} - c \frac{\partial^2 \omega}{\partial x^2} - d \frac{\partial^2 \omega}{\partial x \partial y} - \frac{\partial c}{\partial x} \frac{\partial \omega}{\partial x} - \frac{\partial d}{\partial x} \frac{\partial \omega}{\partial y} - \frac{\partial q}{\partial x} \tag{42}$$

$$\begin{aligned} \frac{\partial^4 \omega}{\partial x^4} = & -\frac{\partial^4 \omega}{\partial x^2 \partial y^2} + c \frac{\partial^3 \omega}{\partial x \partial y^2} - d \frac{\partial^3 \omega}{\partial x^2 \partial y} + \left( c^2 - 2 \frac{\partial c}{\partial x} \right) \frac{\partial^2 \omega}{\partial x^2} \\ & + \left( cd - 2 \frac{\partial d}{\partial x} \right) \frac{\partial^2 \omega}{\partial x \partial y} + \left( c \frac{\partial c}{\partial x} - \frac{\partial^2 c}{\partial x^2} \right) \frac{\partial \omega}{\partial x} \end{aligned} \tag{43}$$

$$\begin{aligned} & + \left( c \frac{\partial d}{\partial x} - \frac{\partial^2 d}{\partial x^2} \right) \frac{\partial \omega}{\partial y} + c \frac{\partial q}{\partial x} - \frac{\partial^2 q}{\partial x^2} \\ \frac{\partial^3 \omega}{\partial y^3} = & -\frac{\partial^3 \omega}{\partial x^2 \partial y} - c \frac{\partial^2 \omega}{\partial x \partial y} \\ & - d \frac{\partial^2 \omega}{\partial y^2} - \frac{\partial c}{\partial y} \frac{\partial \omega}{\partial x} - \frac{\partial d}{\partial y} \frac{\partial \omega}{\partial y} - \frac{\partial q}{\partial y} \end{aligned} \tag{44}$$

$$\begin{aligned} \frac{\partial^4 \omega}{\partial y^4} = & -\frac{\partial^4 \omega}{\partial x^2 \partial y^2} - c \frac{\partial^3 \omega}{\partial x \partial y^2} + d \frac{\partial^3 \omega}{\partial x^2 \partial y} + \left( d^2 - 2 \frac{\partial d}{\partial y} \right) \frac{\partial^2 \omega}{\partial y^2} \\ & + \left( cd - 2 \frac{\partial c}{\partial y} \right) \frac{\partial^2 \omega}{\partial x \partial y} + \left( d \frac{\partial c}{\partial y} - \frac{\partial^2 c}{\partial y^2} \right) \frac{\partial \omega}{\partial x} \\ & + \left( d \frac{\partial d}{\partial y} - \frac{\partial^2 d}{\partial y^2} \right) \frac{\partial \omega}{\partial y} + d \frac{\partial q}{\partial y} - \frac{\partial^2 q}{\partial y^2} \end{aligned} \tag{45}$$

First we insert (42) to (45) in the truncation error term (41) and then substitute the resulting expression for  $\zeta_{i,j}$  in (40) and then apply  $D$ -operators from (18) to (25) so that we will get

$$\begin{aligned} & -e D_x^2 \omega_{i,j} - f D_y^2 \omega_{i,j} + g D_x \omega_{i,j} - o D_y \omega_{i,j} \\ & - d_3 \left( D_x^2 D_y^2 \omega_{i,j} - c D_x D_y^2 \omega_{i,j} - d D_x^2 D_y \omega_{i,j} \right) + w D_x D_y \omega_{i,j} \\ & + \frac{h^2}{12} \left[ c \left( \frac{\partial q}{\partial x} \right) - \left( \frac{\partial^2 q}{\partial x^2} \right) \right] + \frac{k^2}{12} \left[ d \left( \frac{\partial q}{\partial y} \right) - \left( \frac{\partial^2 q}{\partial y^2} \right) \right] - q = 0 \end{aligned} \tag{46}$$

The coefficients in the above equation are,

$$e = 1 + Re \frac{h^2}{12} (Re D_y \psi - 2 D_x) D_y \psi \tag{47}$$

$$f = 1 + Re \frac{k^2}{12} (Re D_x \psi + 2 D_y) D_x \psi \tag{48}$$

$$\begin{aligned} g = & Re D_y \psi + Re \frac{h^2}{12} (D_x - Re D_y \psi) D_x D_y \psi \\ & + Re \frac{k^2}{12} (D_y + Re D_x) D_y^2 \psi \end{aligned} \tag{49}$$

$$\begin{aligned} o = & -Re D_x \psi \\ & + Re \frac{h^2}{12} (-D_x + Re D_y \psi) D_x^2 \psi - Re \frac{k^2}{12} (D_y + Re D_x) D_x D_y \psi \end{aligned} \tag{50}$$

$$w = -Re \frac{h^2}{6} D_x^2 \psi + \frac{k^2}{6} D_y^2 \psi - d_3 Re^2 D_x \psi D_y \psi \tag{51}$$

Upon simplifying the above Equation (46), we will get the fourth order accurate finite difference representation of the vorticity differential Equation (36) as given below.

$$\begin{aligned}
 &\omega_0(-16d_3 + 8h^2f + 8k^2e) + \omega_1(8d_3 - 4hd_3c - 4k^2e + 2hk^2g) \\
 &+ \omega_2(8d_3 - 4kd_3d - 4h^2f + 2h^2ko) + \omega_3(8d_3 + 4hd_3c - 4k^2e - 2hk^2g) \\
 &+ \omega_4(8d_3 + 4kd_3d - 4h^2f - 2h^2ko) + \omega_5(-4d_3 + 2hd_3c + 2kd_3d + hkw) \\
 &+ \omega_6(-4d_3 - 2hd_3c + 2kd_3d - hkw) + \omega_7(-4d_3 - 2hd_3c - 2kd_3d + hkw) \\
 &+ \omega_8(-4d_3 + 2hd_3c - 2kd_3d - hkw) \tag{52} \\
 &= -4h^2k^2Re \cdot Ri \left[ \frac{h^2}{12}(-ReD_y\psi + D_x^2) + \frac{k^2}{12}(ReD_x\psi D_y + D_y^2) + 1 \right] D_x T
 \end{aligned}$$

It may be noted that before implementing the code for Equation (10), the expressions for the quantities  $c$ ,  $d$  and  $q$  should also be replaced by fourth order accurate relations as given below.

$$c_{i,j} = Re \left( D_y\psi - d_2 \frac{\partial^3\psi}{\partial y^3} \right) = Re \left[ D_y + d_2 D_x^2 D_y \right] \psi - Re \left[ d_2 D_y \right] \omega \tag{53}$$

$$d_{i,j} = -Re \cdot Pr \left( D_x\psi - d_1 \frac{\partial^3\psi}{\partial x^3} \right) = -Re \left[ D_x + d_1 D_y^2 D_x \right] \psi - Re \left[ d_1 D_x \right] \omega \tag{54}$$

$$q_{i,j} = -Re \cdot Pr \left( D_x T - d_1 \frac{\partial^3 T}{\partial x^3} \right) = -Re \cdot Pr \left[ D_x + d_1 D_y^2 D_x \right] T - Re \cdot Pr \left[ d_1 D_x \right] \omega \tag{55}$$

### 3.3. Discretization of Energy Equation

Now, the temperature Equation (10) is rewritten as

$$\frac{\partial^2 T}{\partial x^2} + \frac{\partial^2 T}{\partial y^2} + c' \frac{\partial T}{\partial x} + d' \frac{\partial T}{\partial y} = 0 \tag{56}$$

Let us define primed variables  $c'$  and  $d'$  at the grid point  $(i, j)$  as

$$c' = -\frac{Re \cdot Pr}{2} \left( \frac{\partial \psi}{\partial y} \right) \tag{57}$$

$$d' = \frac{Re \cdot Pr}{2} \left( \frac{\partial \psi}{\partial x} \right) \tag{58}$$

Using Equations (14) to (17) together with the above two primed variables in (10), we get discretized version with truncation error term as follows.

$$D_x^2 T_{i,j} + D_y^2 T_{i,j} + c'_{i,j} D_x T_{i,j} + d'_{i,j} D_y T_{i,j} - \gamma_{i,j} = 0 \tag{59}$$

and the truncation error term  $\gamma_{i,j}$  in the previous equation is

$$\begin{aligned}
 \gamma_{i,j} = & - \left[ \frac{c'h^2}{6} \frac{\partial^3 T}{\partial x^3} + \frac{h^2}{12} \frac{\partial^4 T}{\partial x^4} + \frac{d'k^2}{6} \frac{\partial^3 T}{\partial y^3} + \frac{k^2}{12} \frac{\partial^4 T}{\partial y^4} \right]_{i,j} \\
 & + \mathcal{O}(h^4, k^4)
 \end{aligned} \tag{60}$$

Now the higher order derivatives of  $T$  present in the previous expression for truncation error can be eliminated by differentiating the energy Equation (10) with respect to  $x$  and  $y$  to yield the following.

$$\frac{\partial^3 T}{\partial x^3} = -\frac{\partial^3 T}{\partial x \partial y^2} - c' \frac{\partial^2 T}{\partial x^2} - d' \frac{\partial^2 T}{\partial x \partial y} - \frac{\partial c'}{\partial x} \frac{\partial T}{\partial x} - \frac{\partial d'}{\partial x} \frac{\partial T}{\partial y} \tag{61}$$

$$\begin{aligned} \frac{\partial^4 T}{\partial x^4} = & -\frac{\partial^4 T}{\partial x^2 \partial y^2} + c' \frac{\partial^3 T}{\partial x \partial y^2} - d' \frac{\partial^3 T}{\partial x^2 \partial y} + \left[ (c')^2 - 2 \frac{\partial c'}{\partial x} \right] \frac{\partial^2 T}{\partial x^2} \\ & + \left( c' d' - 2 \frac{\partial d'}{\partial x} \right) \frac{\partial^2 T}{\partial x \partial y} + \left( c' \frac{\partial c'}{\partial x} - \frac{\partial^2 c'}{\partial x^2} \right) \frac{\partial T}{\partial x} + \left( c' \frac{\partial d'}{\partial x} - \frac{\partial^2 d'}{\partial x^2} \right) \frac{\partial T}{\partial y} \end{aligned} \tag{62}$$

$$\frac{\partial^3 T}{\partial y^3} = -\frac{\partial^3 T}{\partial x^2 \partial y} - c' \frac{\partial^2 T}{\partial x \partial y} - d' \frac{\partial^2 T}{\partial y^2} - \frac{\partial c'}{\partial y} \frac{\partial T}{\partial x} - \frac{\partial d'}{\partial y} \frac{\partial T}{\partial y} \tag{63}$$

$$\begin{aligned} \frac{\partial^4 T}{\partial y^4} = & -\frac{\partial^4 T}{\partial x^2 \partial y^2} - c' \frac{\partial^3 T}{\partial x \partial y^2} + d' \frac{\partial^3 T}{\partial x^2 \partial y} + \left[ (d')^2 - 2 \frac{\partial d'}{\partial y} \right] \frac{\partial^2 T}{\partial y^2} \\ & + \left( c' d' - 2 \frac{\partial c'}{\partial y} \right) \frac{\partial^2 T}{\partial x \partial y} + \left( d' \frac{\partial c'}{\partial y} - \frac{\partial^2 c'}{\partial y^2} \right) \frac{\partial T}{\partial x} + \left( d' \frac{\partial d'}{\partial y} - \frac{\partial^2 d'}{\partial y^2} \right) \frac{\partial T}{\partial y} \end{aligned} \tag{64}$$

Substituting the set of Equations (61) to (64) in the equation for truncation error (60) and also applying the  $D$  operators from (18) to (25), in the Equation (59) we get

$$\begin{aligned} & \left[ -\zeta D_x^2 - \rho D_y^2 + \varpi D_x + \mathcal{G} D_y + \varepsilon D_x D_y \right] T \\ & - (d_1 + d_2) \left[ D_x^2 D_y^2 - c' D_x D_y^2 - d' D_x^2 D_y \right] T = 0 \end{aligned} \tag{65}$$

where the coefficients  $\zeta, \rho, \varpi, \mathcal{G}, \varepsilon$  appearing in the above equation are

$$\zeta = 1 + d_1 (c')^2 - Re \cdot Pr \cdot d_1 D_x D_y \psi \tag{66}$$

$$\rho = 1 + d_2 (d')^2 - Re \cdot Pr \cdot d_2 D_y^2 \psi \tag{67}$$

$$\varpi = c' + d_1 (c' D_x c' + D_x^2 c') + d_2 (d' D_y c' + D_y^2 c') \tag{68}$$

$$\mathcal{G} = d' + d_1 (c' D_x d' + D_x^2 d') + d_2 (d' D_y d' + D_y^2 d') \tag{69}$$

$$\varepsilon = Re \cdot Pr \left[ -d_1 D_x^2 + d_2 D_y^2 \right] \psi - (d_1 + d_2) \cdot (c' d') \tag{70}$$

It may be noted that before implementing the code for Equation (65), the expressions for primed quantities  $c'$  and  $d'$  should also be replaced by fourth order accurate relations as given below.

$$\begin{aligned} (c')_{i,j} = & -Re \cdot Pr \left( D_y \psi - d_2 \frac{\partial^3 \psi}{\partial y^3} \right) \\ = & Re \cdot Pr \left[ d_2 D_y \right] \omega - Re \cdot Pr \left[ D_y + d_2 D_x^2 D_y \right] \psi \end{aligned} \tag{71}$$

$$\begin{aligned} (d')_{i,j} = & Re \cdot Pr \left( D_x \psi - d_1 \frac{\partial^3 \psi}{\partial x^3} \right) \\ = & Re \cdot Pr \left[ d_1 D_x \right] \omega + Re \cdot Pr \left[ D_x + d_1 D_y^2 D_x \right] \psi \end{aligned} \tag{72}$$

and the constants  $d_1, d_2$  and  $d_3$  are already defined in Equations (33) to (35). Finally, we have arrived at a set of three coupled discretized Equations (32), (52) and (65) whose accuracy is  $\mathcal{O}(h^4, k^4)$ .

### 4. Implementation of Numerical Scheme

The set of coupled discretized equations as mentioned above is applied to each grid point in the computational domain and this produces a large linear sparse

system which exhibits diagonal dominance. Therefore we could use the multigrid method with Gauss-Seidel iteration as relaxer. We have chosen to use the multigrid method because it accelerates convergence when compared to using stand-alone iterative procedures. The set of grids used are  $32 \times 32$ ,  $64 \times 64$ ,  $128 \times 128$ ,  $256 \times 256$  and  $512 \times 512$ . If the solution  $\Psi$  of a particular equation in the finest grid  $512 \times 512$  is denoted by  $\Psi^{(512)}$  then the solution of the same equation in the next finer grid  $256 \times 256$  will be denoted by  $\Psi^{(256)}$ . We have used the simplest of the restriction operator, called the injection operator  $\mathcal{I}$  which simply copies the finest grid solution to the next finer grid (or the coarsest grid as the case may be) at grid points which are common to both grid levels. In **Figure 2**, the stars denote boundary points and the circles are points that are common to two different grids. The injection operation involves equating the values at circles in  $4 \times 4$  grid to the circles in  $8 \times 8$  grid (**Figure 2**). The reverse operation to injection is known as prolongation operation  $\mathcal{P}$ . The prolongation operation is done for the points shown as square in **Figure 2** as follows. The value of  $\Psi$  at grid point  $B$  in  $4 \times 4$  grid is equal to the value of  $\Psi$  at  $A$  in  $8 \times 8$  grid, which is written as,

$$\left[ \Psi^{(8 \times 8)} \right]_{2i, 2j} = \left[ \Psi^{(4 \times 4)} \right]_{i, j} \tag{73}$$

In general, if the finest grid is represented as  $k$  and the next finer grid is represented as  $k-1$  then the above equation is rewritten as,

$$\left[ \Psi^{(k)} \right]_{2i, 2j} = \left[ \Psi^{(k-1)} \right]_{i, j} \tag{74}$$

The value of  $\Psi$  in  $8 \times 8$  grid at point  $C$  grid is equal to the average of values of  $\Psi$  at  $B$  and  $D$  in  $4 \times 4$  grid. This is expressed in general as

$$\left[ \Psi^{(k)} \right]_{2i+1, 2j} = \frac{\left[ \Psi^{(k-1)} \right]_{i, j} + \left[ \Psi^{(k-1)} \right]_{i+1, j}}{2} \tag{75}$$

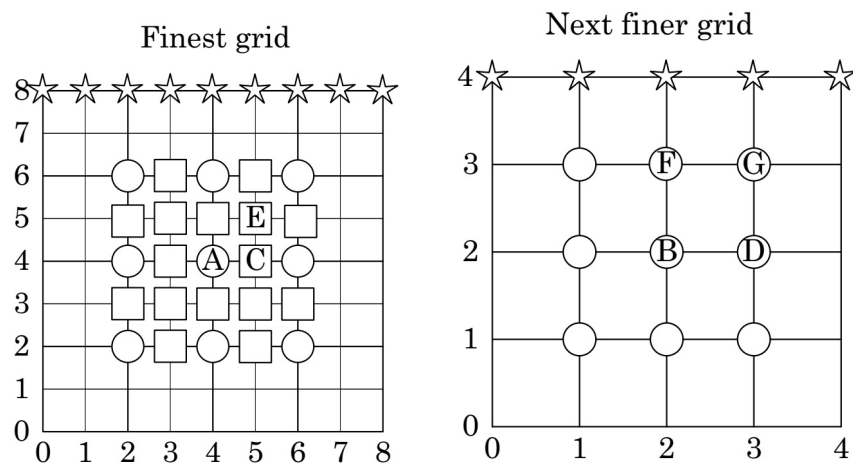


**Figure 2.** Schematic of two-level grids used for illustrating the injection and prolongation operations. Circles are points common to both grids. Stars are boundary (or known) points. The squares are the points at which the value is to be found using the prolongation operation.

Here  $k$  means finest grid and  $k - 1$  means next finer (or coarsest) grid. Similarly, the values at all other square points are obtained using the following averaging scheme.

$$\left[ \Psi^{(k)} \right]_{2i,2j+1} = \frac{1}{2} \left( \left[ \Psi^{(k-1)} \right]_{i,j} + \left[ \Psi^{(k-1)} \right]_{i,j+1} \right) \tag{76}$$

$$\begin{aligned} \left[ \Psi^{(k)} \right]_{2i+1,2j+1} = & \frac{1}{4} \left( \left[ \Psi^{(k-1)} \right]_{i,j} + \left[ \Psi^{(k-1)} \right]_{i+1,j} \right. \\ & \left. + \left[ \Psi^{(k-1)} \right]_{i,j+1} + \left[ \Psi^{(k-1)} \right]_{i+1,j+1} \right) \end{aligned} \tag{77}$$

The above set of Equations (74) to (77) comprise the 9-point prolongation operator [38]. The three coupled discretized Equations (32), (52) and (65) are relaxed simultaneously and the boundary conditions are incorporated implicitly. A point Gauss-Seidel iterative scheme is used for the relaxation procedure. This pre-smoothing iterations are carried out on the finest grid. Then we restrict (or inject) the residual on the coarsest grid. Let the residual be denoted by  $r$ . By solving the matrix equation  $Ae = r$  we get the error in the coarsest grid. This error  $e$  is prolonged to the finest grid and then added to  $\Psi_{old}$  as below

$$\Psi_{\text{coarse grid corrected}} = \Psi_{old} + \mathcal{P}[e] \tag{78}$$

where  $\mathcal{P}$  is the prolongation operator (for more details, see [38]). After performing a few post-smoothing operation, one multigrid cycle is completed. This procedure is repeated until the following condition is satisfied for convergence.

$$\frac{|X^{n+1} - X^n|}{|X^{n+1}|} \leq 10^{-7} \tag{79}$$

where  $X$  is any of  $\psi, \omega, T$  and  $n$  is the iteration number.

### Treatment of Boundary Points

At all the boundary points, fourth order accurate one sided finite-difference formula is used for derivatives involving  $\psi, \omega$  and  $T$ . The first derivative of temperature along all points in left vertical wall is

$$T(1, j) = \frac{1}{25} [48T(2, j) - 36T(3, j) + 16T(4, j) - 3T(5, j)] \tag{80}$$

and similarly the same for the right vertical wall is expressed as

$$T(m+1, j) = \frac{1}{25} [-48T(m, j) + 36T(m-1, j) - 16T(m-2, j) + 3T(m-3, j)] \tag{81}$$

A fourth order backward difference scheme is used to find  $\omega$  at top moving wall.

$$\begin{aligned} \omega(i, n+1) = & \frac{-1}{12h^2} [45\psi(i, n+1) - 154\psi(i, n) + 214\psi(i, n-1) \\ & - 156\psi(i, n-2) + 61\psi(i, n-3) - 10\psi(i, n-4)] \end{aligned} \tag{82}$$

Similarly, the fourth order one sided finite difference is used to find  $\omega$  at all other walls

$$\omega(1, j) = \frac{-1}{12h^2} [45\psi(1, j) - 154\psi(2, j) + 214\psi(3, j) - 156\psi(4, j) + 61\psi(5, j) - 10\psi(6, j)] \quad (83)$$

$$\omega(m+1, j) = \frac{-1}{12h^2} [45\psi(m+1, j) - 154\psi(m, j) + 214\psi(m-1, j) - 156\psi(m-2, j) + 61\psi(m-3, j) - 10\psi(m-4, j)] \quad (84)$$

$$\omega(i, 1) = \frac{-1}{12h^2} [45\psi(i, 1) - 154\psi(i, 2) + 214\psi(i, 3) - 156\psi(i, 4) + 61\psi(i, 5) - 10\psi(i, 6)] \quad (85)$$

## 5. Results and Discussion

The flow characteristics together with thermal fields are computed for different  $Re$ ,  $Pr$  and  $Gr$  (or equivalent  $Ri$ ). The density variation is induced through a linearly varying top moving wall. The effect of mixed convection is analyzed through streamlines, isothermal contours and Nusselt number for  $100 \leq Re \leq 3000$ ,  $0.015 \leq Pr \leq 10$  and Grashof number  $10^2 \leq Gr \leq 10^6$  and further explained through contours of components of velocity and temperature in the mid-cross-section of the cavity. At the end, the numerical accuracy of the proposed scheme is established.

### 5.1. Code Validation and Grid Independence Study

To validate our coding we have run the program with aiding and opposing shear boundary conditions available in the literature. The validations are done for various values of  $Re$  and a fixed value of  $Pr = 0.73$ . The parameter used to study the mixed convection is Richardson number  $Ri$  which is also equal to  $Gr/Re^2$ . The case of  $Ri \ll 1$  belongs to the class of forced convection and if  $0.1 \leq Ri \leq 10$  we may describe as mixed convection. **Table 2** shows the grid independence results for  $Gr = 0$  case in terms of values of streamfunction,  $\psi$ , and vorticity,  $\omega$  which are evaluated at the centers of primary and two secondary vortices for different values of  $Re$ . Here a fluid with a constant  $Pr = 0.73$  is considered. In our computation, the coarser grids are  $64 \times 64$ ,  $128 \times 128$ , and  $256 \times 256$  while the finest grid used in the present study is  $512 \times 512$ . From the tabulated data, it is seen that  $256 \times 256$  grid is found to be optimum. Further refining of grids will not give more accuracy because the accuracy of the numerical scheme is decided by method of discretization and not by the fineness of the grid. The advantage with the present higher order scheme is that we can achieve the accurate results in smaller grid itself. **Table 3** shows the location of primary vortex and flow parameters such as streamfunction and vorticity in different grids, and they are compared with the literature data that include data that might have been computed using a lower order finite difference method [1] [13] [14] [39] [40] [41], and from the tabulated data it is observed that there is a very good agreement among different reports. In particular, the results of [14] is matching to a good degree with that of our computed value. In

**Table 2.** The grid independence study of in terms of stream function and vorticity at the centres of primary and secondary vortices located at bottom left (BL) and bottom right (BR) respectively.

<i>Re</i>	<i>Grid</i>	<i>Centre of primary vortex</i>		<i>Centre of secondary vortex, BL</i>		<i>Centre of secondary vortex, BR</i>	
		$\psi$	$\omega$	$\psi$	$\omega$	$\psi$	$\omega$
100	64 × 64	0.10352	3.16686	1.33E-06	1.97E-02	1.25E-05	3.89E-02
	128 × 128	0.10351	3.1687	1.74E-06	1.57E-02	1.27E-05	3.31E-02
	256 × 256	0.10352	3.16098	1.79E-06	1.60E-02	1.27E-05	3.69E-02
	512 × 512	0.10352	3.16646	1.76E-06	1.70E-02	1.27E-05	3.46E-02
1000	64 × 64	0.11853	2.06526	2.07E-04	0.4442	1.74E-03	1.10526
	128 × 128	0.11881	2.06641	2.31E-04	0.36691	1.73E-03	1.14018
	256 × 256	0.11893	2.06763	2.33E-04	0.34489	1.73E-03	1.13901
	512 × 512	0.11894	2.06778	2.33E-04	0.35653	1.73E-03	1.11469
5000	64 × 64	0.12009	1.94912	1.09E-04	1.13579	3.16E-03	2.50248
	128 × 128	0.12103	1.94569	1.19E-04	1.27903	3.13E-03	2.54565
	256 × 256	0.1219	1.93715	1.35E-04	1.41837	3.07E-03	2.70553
	512 × 512	0.1222	1.94038	1.38E-04	1.51437	3.07E-03	2.74876

**Table 3.** Comparison of computed values of streamfunction, vorticity and coordinates (*x*, *y*) of primary vortex with literature.

<i>Re</i>	<i>Reference</i>	<i>Grid</i>	<i>x</i>	<i>y</i>	$\psi$	$\omega$	
1000	Ghia <i>et al.</i> (1982)	128 × 128	0.5313	0.5625	0.117929	2.04968	
	Zhang (2003)		0.46875	0.5625	0.118806	2.066777	
	Bottella and Peyret (1998)		0.4692	0.5625	0.118937	2.06775	
	Bruneau and Saad (2005)		0.46875	0.5625	0.11786	2.0508	
	Cheng (2010)		0.46875	0.5625	0.116874	2.064753	
	Present (4 <sup>th</sup> order scheme)		0.53125	0.5625	0.118812	2.066411	
	Erturk and Gokcol (2006)		600 × 600	0.53	0.565	0.118938	2.06776
	Present (4 <sup>th</sup> order scheme)			0.53	0.565	0.118936	2.067726
	Ghia <i>et al.</i> 1982)			0.5165	0.5469	0.120377	1.9886
	3200		Zhang (2003)	128 × 128	0.484375	0.539063	0.120157
Cheng (2010)		0.484375	0.539063		0.119845	1.947966	
Present (4 <sup>th</sup> order scheme)		0.515625	0.539063		0.121136	1.95844	
Zhang (2003)		0.484375	0.539063		0.118121	1.906214	
Cheng (2010)		0.484375	0.539063		0.118224	1.909011	
Present (4 <sup>th</sup> order scheme)		0.515625	0.539063		0.121038	1.945688	
5000	Ghia <i>et al.</i> (1982)	256 × 256	0.4883	0.5352	0.118966	1.86016	
	Bruneau and Saad (2005)		0.43438	0.53516	0.12064	1.9125	
	Present (4 <sup>th</sup> order scheme)		0.515625	0.535156	0.121902	1.937153	
	Erturk and Gockol (2006)		600 × 600	0.515	0.535	0.122216	1.940547
	Present (4 <sup>th</sup> order scheme)		0.515	0.535	0.122216	1.940524	

order to perform validation for heat transfer studies, we have exclusively run the code with the boundary condition  $T = 1$  for the top moving wall and the results are shown in **Table 4** and the data is compared with literature [15] [42] [43]. Essentially there is hardly a 0.03% variation among other reported values that has been computed using some fourth order scheme and 0.1% variation among second order accurate computations.

## 5.2. Flow Structure and Isotherms

Experimental investigation of lid-driven flow and its effect on density variations show that [44] [45] the flow consists mainly of a central recirculating zone with one downstream secondary eddy (DSE) and one upstream secondary eddy (USE). Additional secondary eddy may be formed if the Reynolds number is suitably high (**Figure 3**). Experimentally it is also known that if the  $Re > 3300$  the flow first becomes three-dimensional and later leads to turbulent cavity flow. Starting with low  $Re$  case, a fluid with  $Pr = 0.73$  is taken and the **Figure 3** shows streamlines and temperature isotherms for increasing buoyancy with  $Gr = 100, 10^4$  and  $10^5$  respectively from top to bottom. The dashed lines in the streamlines correspond to flow in clockwise direction while the anticlockwise flow is shown as solid lines. In the present configuration, both shear stress and density variation are created near the upper moving lid because the bottom lid is held at a lower constant temperature and the side vertical walls are thermally insulated. This cavity flow configuration is in contrast with other studies reported in the literature [15] [46]. Other notable studies where the bottom wall is colder than the top moving lid are [42] [47] but however, the vertical walls are not necessarily held adiabatic. The top plot in **Figure 4** correspond to negligible

**Table 4.** Comparison of average Nusselt number  $N_m$  in the top moving wall where the boundary condition imposed is  $T = 1$  for the fluid flow with  $Pr = 0.73$ .

<i>Re</i>	<i>Grid</i>	<i>Authors</i>	<i>Nm</i>	<i>Nm</i>
100	128 × 128	Iwatsu <i>et al.</i> (1993)	1.94	1.34
		Present work	2.11	1.44
400	100 × 100	Sharif (2007)	4.05	3.82
		Present work	4.28	4.04
400	128 × 128	Iwatsu <i>et al.</i> (1993)	3.84	3.62
		Cheng (2011)	4.14	3.9
1000	100 × 100	Present work	4.25	4.01
		Sharif (2007)	6.55	6.5
1000	128 × 128	Present work	6.93	6.88
		Iwatsu <i>et al.</i> (1993)	6.33	6.29
1000	128 × 128	Cheng (2011)	6.73	6.68
		Present work	6.92	6.87

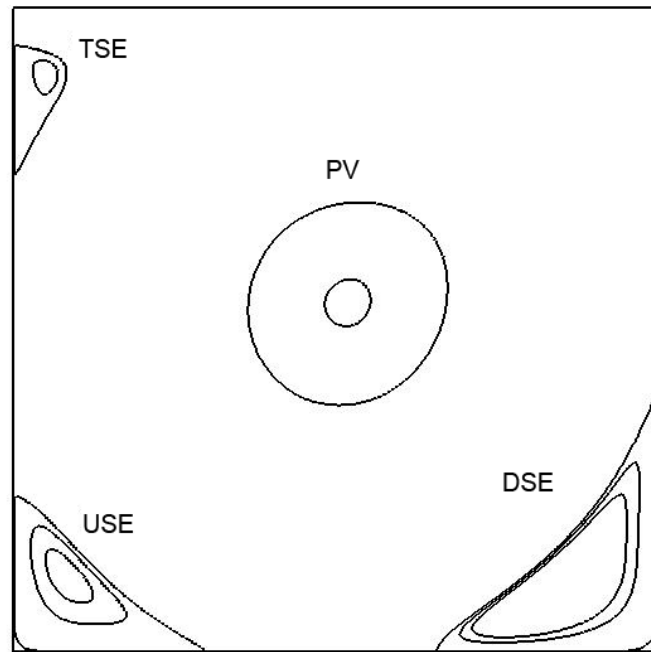


**Figure 3.** Schematic of streamlines with possible recirculation regions. PV is the primary vortex, USE is upstream secondary eddy, DSE is the downstream secondary eddy and TSE is the top left secondary eddy.

buoyant force  $Ri = 0.01$  and the flow is due mainly to the shear force provided by moving lid and hence we compare the positions of primary and additional eddies against the literature [48].

From the isotherm contours of **Figure 4**, (right side plots) it is observed that the temperature of the fluid in the cavity for  $Ri = 0.01$  case has non-uniform layered structure and this has resulted due predominantly to forced convection effects. If we come to the mixed convection region  $Ri \geq 1$ , a considerable change in both flow structure and thermal fields can be seen (middle and bottom plots of **Figure 4**). For  $Re = 100$  case, the thermal boundary layer thickness with respect to bottom wall increases as  $Ri$  increases. As the increase of buoyant force by increasing  $Ri$ , the size of the secondary BR (bottom right) vortex decreases. Simultaneously the BL (bottom left) secondary vortex increases so as to form two analogous large counter rotating vortices that occupies the entire cavity. **Table 5** shows the growth, merging and mixing of secondary vortices with the increase of Grashof number for different values of  $Re$ . From the table it is noted that the USE and DSE are merges for Richardson number  $Ri \geq 1$ . Even though the flow structure changes dramatically, the temperature distribution in the layers of the fluid have nearly a flat or uniform thermal gradient. This is in contrast to thermal distribution for low  $Ri$  case where large amount of fluid is nearly isothermal. When the Richardson number is significant, that is, when mixed convection plays a role, the size of the USE on bottom left corner increases at the expense of DSE which is located on the bottom right side of the cavity. This could be due to the suppression of adverse pressure gradient which in turn is due to the thermal gradient existing between top and bottom walls.

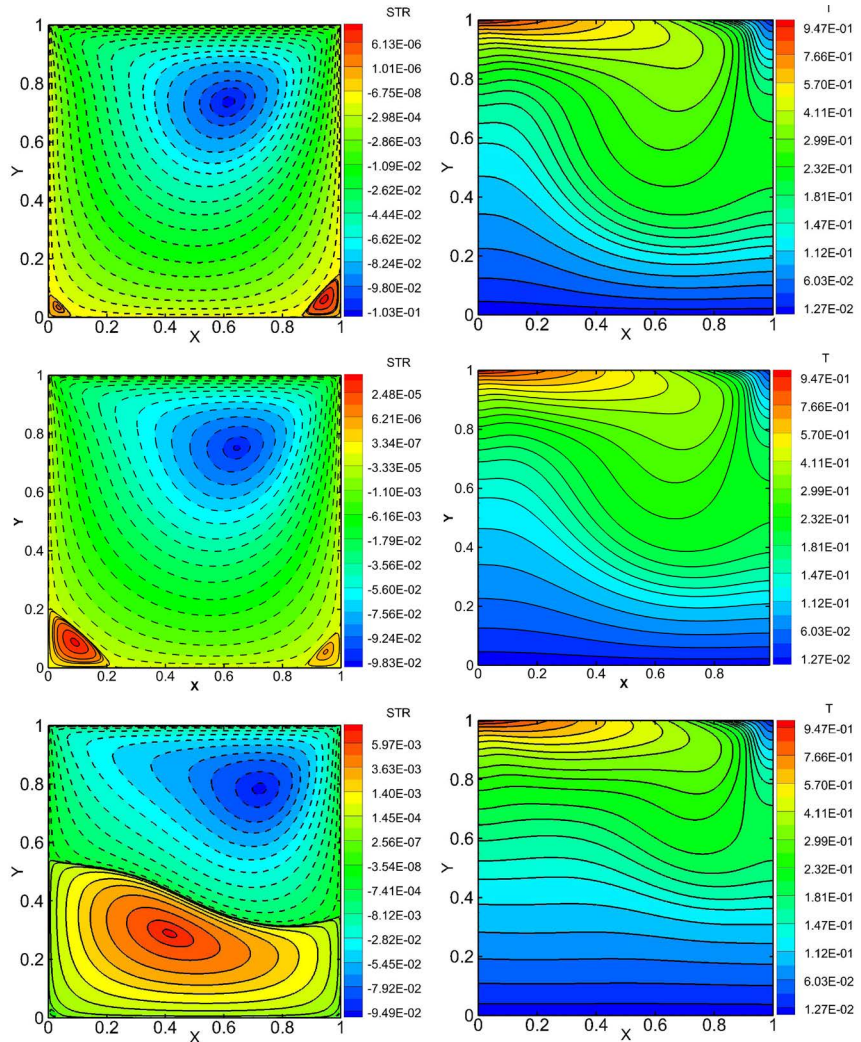


**Figure 4.** Streamfunction contours (left) and isotherms (right) for  $Ri = 0.01, 1$  and  $10$  respectively (top to bottom) for a flow of fluid with  $Re = 100$  and  $Pr = 0.73$ . Equivalent values of  $Gr$  are  $10^2, 10^4$  and  $10^5$  respectively from top to bottom.

**Table 5.** Growth, degradation and merging of secondary vortices due to increased mixed convection.

Re	Gr	Ri	Area of USE	Area of DSE	Area of TSE
100	102	0.01	0.28E-2	0.98E-2	0
	104	1	2.10E-2	0.78E-2	0
	106	10	USE and DSE merges		
400	104	0.0625	0.90E-2	3.70E-2	0
	105	0.625	4.50E-2	2.60E-2	0
	106	6.25	USE and DSE merges		
1000	104	0.01	1.90E-2	5.20E-2	0
	105	0.1	2.10E-2	4.90E-2	0
	106	1	USE and DSE merges		
3000	103	0.0011	3.60E-2	7.00E-2	0.080E-2
	104	0.011	3.70E-2	6.60E-2	0.085E-2
	105	0.11	4.30E-2	5.70E-2	0.090E-2

When Richardson number is increased to  $Ri = 10$ , a significant change in the fluid flow is observed, wherein the USE grows until it occupies nearly half of the cavity, which is attributed to the buoyancy effects. The direction of flow in this eddy is opposite to that of the main or primary vortex. In addition, the center of primary vortex moves towards the right wall as  $Ri$  increases. The size of the clockwise and anticlockwise rotating vortices have same size, which shows that the effect of shear driven forced convection effect and buoyancy driven convection effects shows equal strength. The thermal contours have more shift than  $Ri = 1$  case of **Figure 4**, towards the top lid. The thermal stratification of fluid is visible for  $Ri = 10$  case than the other two cases ( $Ri = 0.01$  and  $Ri = 1$ ). In this range the conduction effect of fluid also plays a vital role. Most of the heat transfer occurring near the stratified fluid is due to conduction, whereas the convection is dominant near the top sliding wall. While considering the recirculation at the middle and bottom of the cavity, the streamlines are more than two-order of magnitude smaller than top sliding wall, which shows the fluid is almost stagnant in the stratified fluid towards the bottom region. The streamlines and isotherms for  $Re = 400$  is plotted in **Figure 5**. When  $Re$  is increased to 400, the corresponding growth of secondary vortices are observed. The middle plot of **Figure 5** shows a growth of secondary upstream vortex and degradation of secondary downstream vortex is observed. Also, a small shift in the position of primary vortex towards the downstream flow region is noticed. The isotherms for weak mixed convection ( $Ri = 0.0625$ ) show that the heat transfer in a more-or-less uniform layered structure till it reaches the center of primary vortex. If  $Ri$  is increased by ten times, to  $Ri = 0.625$ , the thermal gradients are reduced but still the isotherm structure is retained. For strong convection case of  $Ri = 6.25$ , it is observed that the sudden growth of upstream secondary vortex due to the increase of unfavorable pressure gradient and the complete suppression of downstream secondary vortex due to the decrease of shear force by the increase of temperature in the downstream makes a favorable pressure gradient. Interestingly a clockwise small vortex forms on the apex of vertical wall near the lid in the downstream region. This is due to the formation of stagnant pressure by the friction loss in the primary vortex itself. Also noted that primary vortex shifts towards the bottom region of the cavity. The temperature distribution is more towards the bottom surface of the cavity. Stagnant layers of fluids is visible in the upstream region. The similar effect is observed for  $Re = 1000$ , where a clockwise vortex formed in the downstream vertical wall and stationary bottom surface **Figure 6** (bottom plot). The changes are insignificant for higher  $Re = 3000$  for all values of  $Gr$  with the fixed case of  $Pr$  **Figure 7**. The clustered temperature isotherms near the top and bottom walls indicates that an large change in the gradient of temperature with respect to normal to the direction of the surface. Whereas the temperature in the recirculation region, the clustering of contours are weak. Hence the temperature gradient is very small indicating that hot fluid is mixed with the cold fluid in that region. In the case of  $Re = 3000$ , the velocity of the fluid is high, hence the mixing of fluid due to

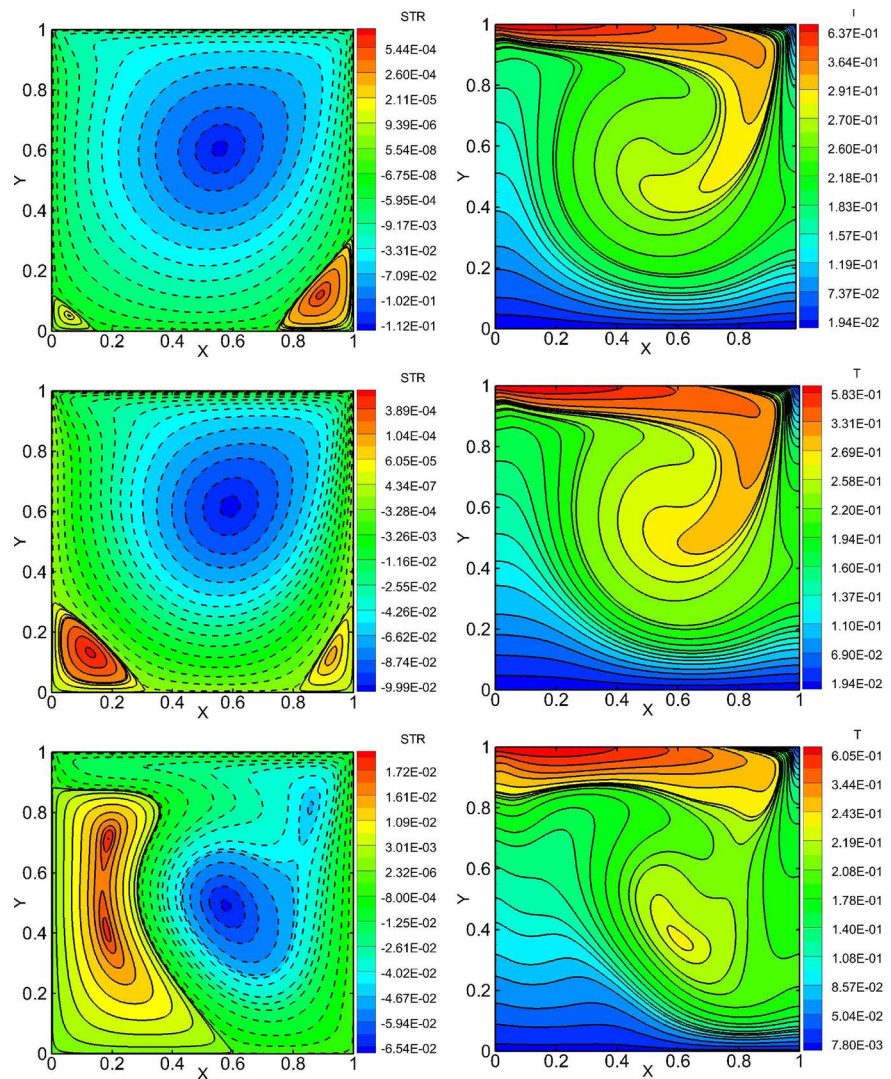


**Figure 5.** Streamfunction contours (left) and isotherms (right) for the flow of fluid with  $Re = 400$  and  $Pr = 0.73$ . Here  $Ri = 0.0625$ ,  $0.625$  and  $6.25$  respectively (top to bottom) or equivalently,  $Gr = 10^4, 10^5$  and  $10^6$  respectively.

shear effect is more significant than buoyancy effect.

The influence of  $Pr$  in flow dynamics and heat transfer is shown in the **Figure 8**. The flow features inside the cavity remains almost unaltered while increasing the Prandtl number for the forced convective heat transfer ( $Ri \ll 1$ ). From the figure, the position and the size of primary and secondary vortices are unaltered with the increase of  $Pr$ , which indicates that flow dynamics is independent of  $Pr$  due to the absence of buoyancy force on the flow for low range of Richardson numbers. The temperature distribution inside the cavity is shown on the right side of the **Figure 8** and show that heat transfer properties are significantly changes with  $Pr$ . The thermal boundary layer thickness on bottom and top surface of the cavity (at very low  $Pr$ ) develops in a layered structure in a stratified manner. While increasing  $Pr$ , the temperature isotherms show that heat transfer extends to the entire region of the cavity together with a thinning

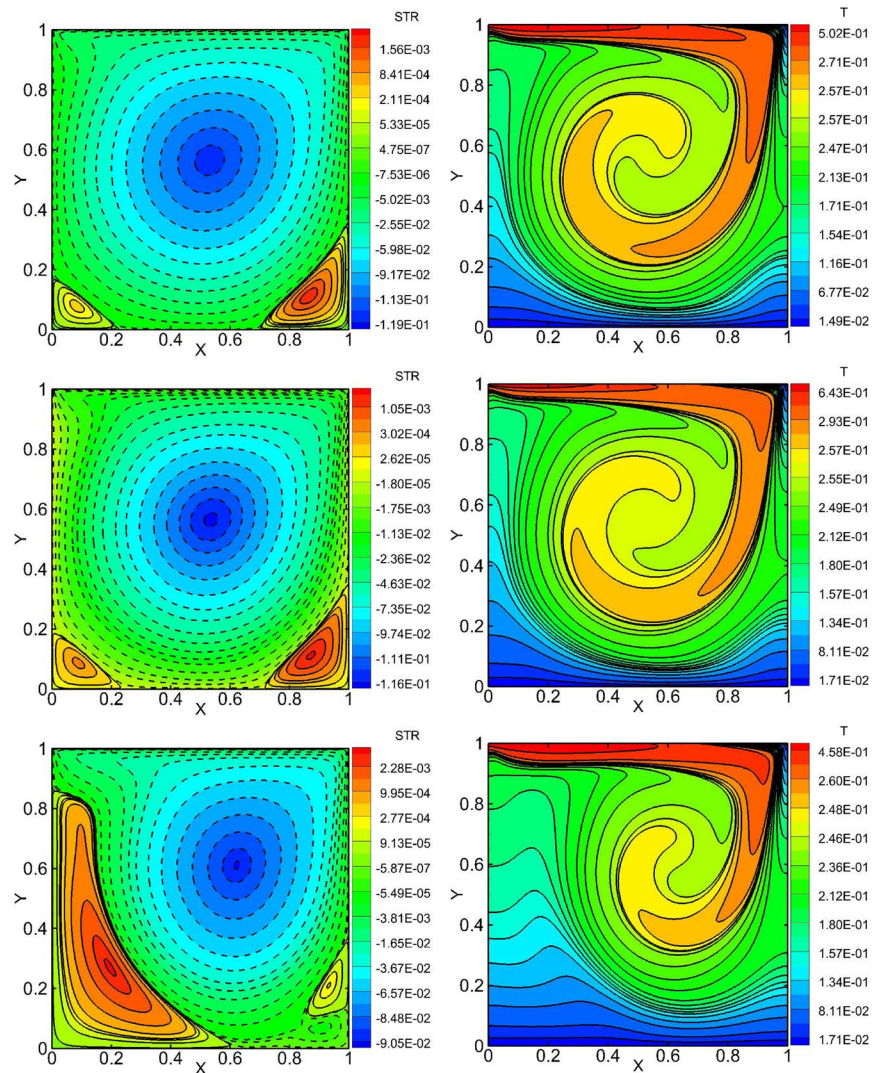


**Figure 6.** Streamlines (left) and isotherms (right) for a fluid flow  $Re = 1000$  and  $Pr = 0.73$ . Here  $Ri = 0.01, 0.1$  and  $1$  respectively (top to bottom) or equivalently  $Gr = 10^4, 10^5$  and  $10^6$ .

effect of thermal boundary layer on the top and bottom surface of the cavity. The numerical experiments are carried out with the increase of  $Ri$  from  $10^4$  to  $10^6$  which is shown in **Figure 9** and a significant change of flow and heat transfer is observed due to large buoyancy force. For small values of  $Pr$  the effect is same as that of **Figure 8**. While increasing Prandtl number, the downstream secondary eddy degrades and the upstream secondary eddy enlarges. Due to linear heating of top wall, maximum heat on the left portion of lid ( $x < 0.5$ ) moves towards the downstream region of the cavity and hence the USE grows. At the same time buoyancy opposes the primary core flow and affects the upstream boundary layer to detach from the wall. For high  $Pr$  flows, clockwise recirculation zone is formed on the left wall. For  $Pr \ll 1$ , the heat transfer in the cavity is due to conduction, shows a thick boundary layer all over the cavity resulting a mild change of temperature produces a feeble buoyant force. For  $Pr \gg 1$ , the

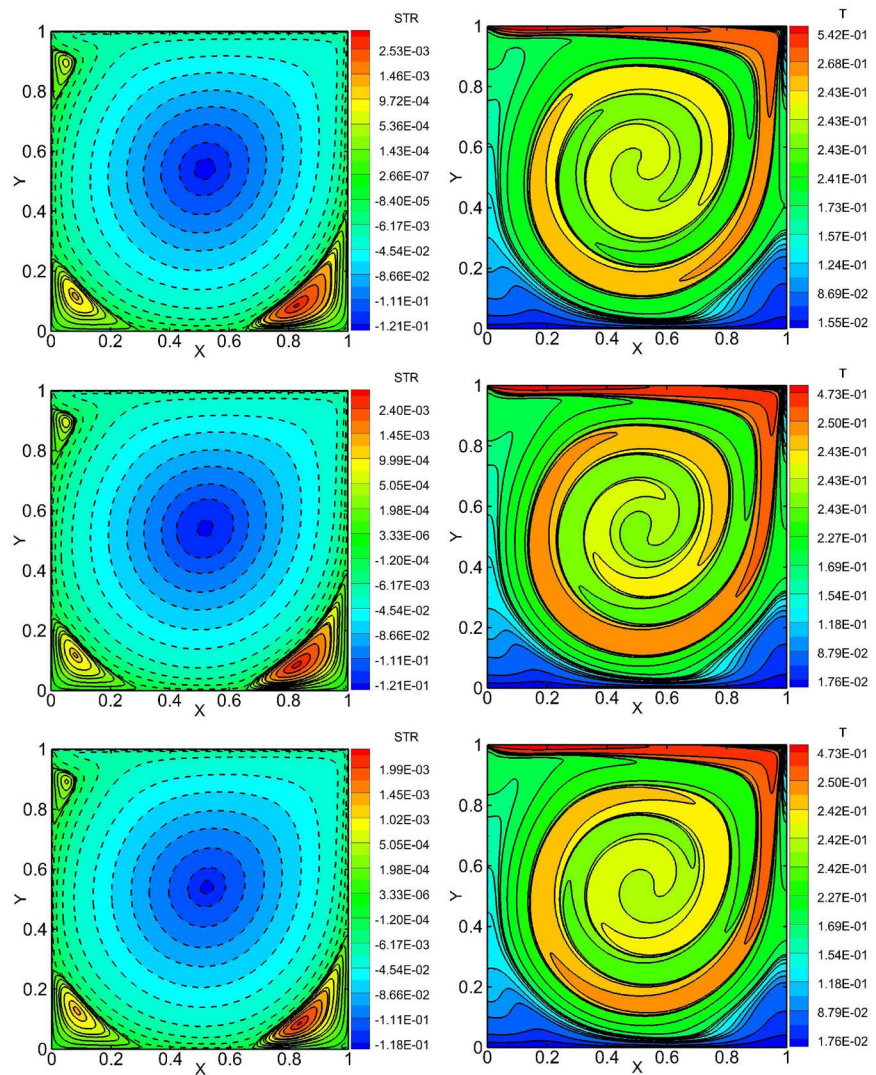


**Figure 7.** Streamlines (left) and isotherms (right) for a fluid flow with  $Re = 3000$  and  $Pr = 0.73$ . Here  $Ri = 0.0011$ ,  $0.011$  and  $0.11$  respectively (top to bottom) or equivalently  $Gr = 10^3, 10^4$  and  $10^5$ .

heat transfer is mainly due to convective effect and the fluid is well mixed in the core of the cavity, hence the buoyant effect exhibits near the walls of the cavity. This makes the degradation of downstream eddy and upgradation of upstream secondary vortex. The reverse will happen for a gravitationally unstable condition [46], where they observed the degradation of upstream secondary vortex and growth of downstream secondary vortex.

Contours of the horizontal and vertical components of velocity  $u$  and  $v$  are plotted in **Figure 10** and **Figure 11** for  $Re = 100$  and  $1000$  respectively. In the case of  $Re = 100$  (**Figure 10**), we could see that the vertical components of velocity  $V$  is modified to a great extent in the left half of the cavity because of the nature of buoyancy which is  $(1-x)$  in our case. Consequently, the density variations are more in left half and they are least in the right half of the cavity. This leads a way to develop two large circulations in opposite directions as seen in

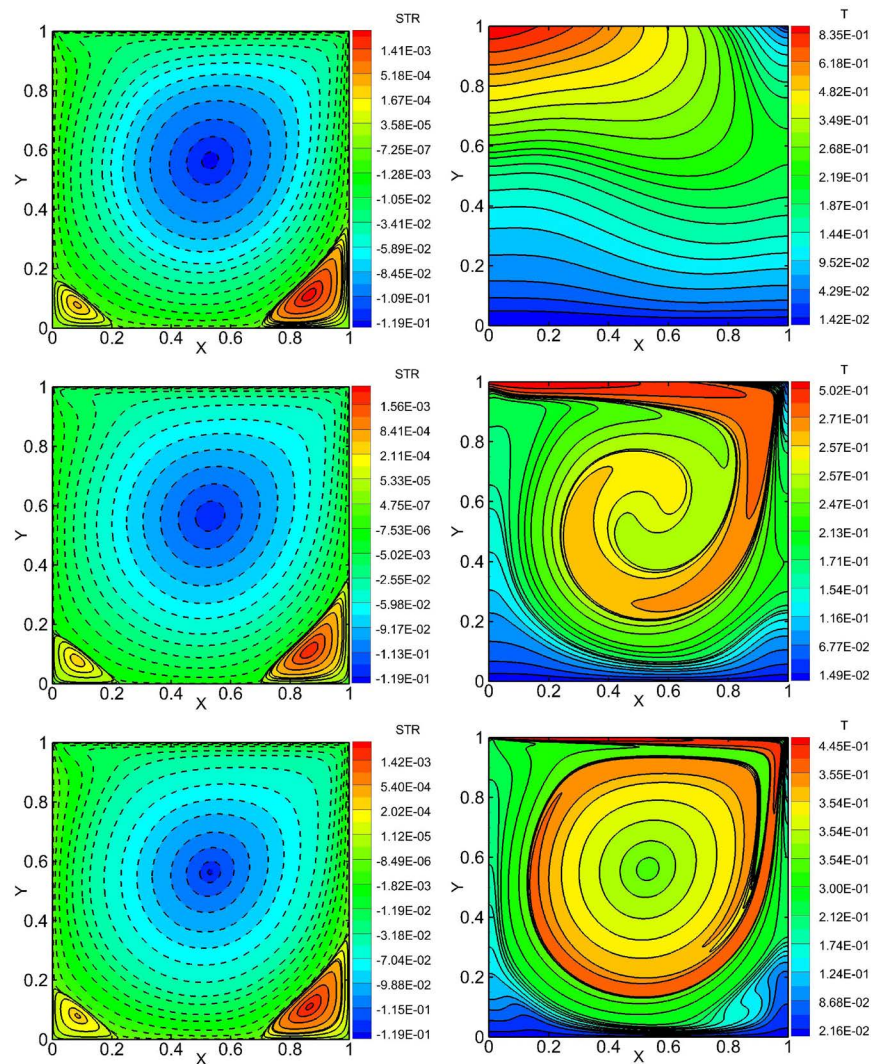


**Figure 8.** For a minimal buoyancy force  $Ri = 0.01$ , the effect of  $Pr$  on the streamlines (left) and temperature isotherms (right) for the flow of fluid with  $Re = 1000$  are shown. Here  $Pr = 0.015, 0.73$  and  $7$  respectively (top to bottom). Equivalent Grashof number is  $Gr = 10^4$ .

bottom left of **Figure 4**. For the case of  $Re = 1000$  (**Figure 11**) however, the minimal viscous force causes the formation of multiple recirculation region. It is also noted that, both velocity components are responsible for the emergence of corner vortices. While increasing  $Re$  the growth of secondary vortices are visible to both velocity components, this effects are due to the conventional flows in a lid-driven cavity. Also the contour lines are pushed towards the top region of the cavity. Due to the push of buoyant force against the gravity, USE grows and finally it form a separate cell near the bottom region of the cavity in the horizontal velocity component, which is visible in the **Figure 11** (bottom left). It is also noted that the horizontal components of velocity undergoes changes as high as three orders of magnitude within the cavity.

Cross sectional profiles of velocity and temperature **Figure 12** shows the vertical ( $v$ ) and horizontal ( $u$ ) components of velocities along the  $x$  and  $y$  directions

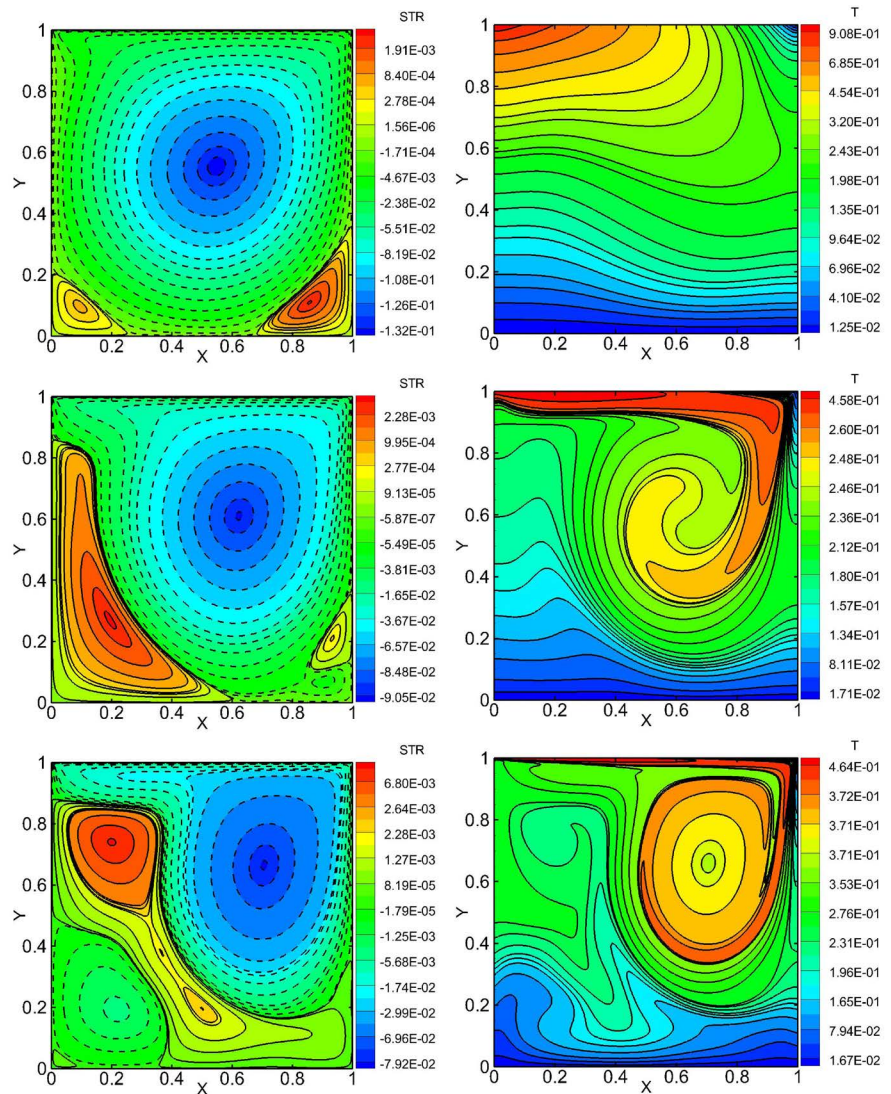


**Figure 9.** For a fairly large buoyancy force  $Ri = 1$ , the effect of  $Pr$  on the streamlines (left) and temperature isotherms (right) for the flow of fluid with  $Re = 1000$  are shown. Here  $Pr = 0.015, 0.73$  and  $7$  respectively (top to bottom). Equivalent Grashof number is  $Gr = 10^6$ .

along vertical center line and horizontal mid-heights respectively. The dash-dot lines of **Figure 12** show the flow in forced convective range. In this case, the velocity is maximum near the walls and the fluid is stagnant in center region of the cavity. This is the expected behavior of lid-driven cavity flow in the absence of buoyant force. In other cases, the velocity changes considerably. **Figure 13** shows the variation of velocity with  $Gr$  (top plot) and  $Pr$  (bottom plot) respectively. From the top plot it is clear that while increasing buoyancy effect the fluid tends to degrade the shear action by moving the line closely towards the stagnant line. Prandtl number have vital effect to pull the fluid to stagnant which is visible from the bottom plot. **Figure 14** shows the temperature profile along vertical and horizontal directions at horizontal mid-length and vertical mid-height for different values of  $Gr$  and  $Re$  respectively. All curves shows

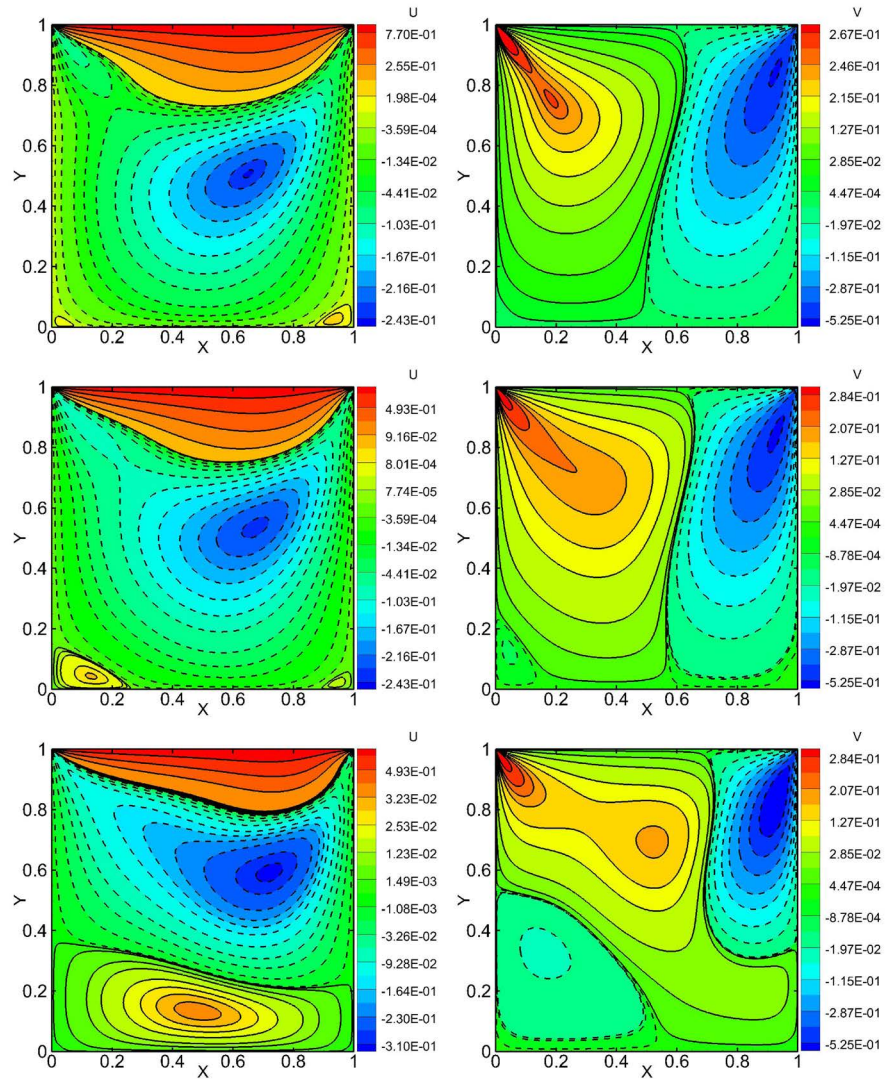


**Figure 10.** Contours of velocity components  $U$ (left) and  $V$ (right) for  $Ri = 0.01, 1$  and  $10$  respectively (top to bottom) for a flow of fluid with  $Re = 100$  and  $Pr = 0.73$ . Equivalent values of  $Gr$  are  $10^2, 10^4$  and  $10^5$  respectively from top to bottom. Here  $U$  is the horizontal component and  $V$  is the vertical component.

minimum temperature at bottom wall and maximum at top wall. In the case of  $Ri \gg 1$  (continuous line plot), for a fixed  $Re$ , temperature distribution shows a linear variation along vertical direction due to the fact that the fluid inside the cavity is almost stagnant which is seen in the **Figure 14** (top left,  $Re = 100$ ). Hence the gradient of temperature is pronounced. Same variation is observed along the horizontal direction **Figure 14** (top right,  $Re = 100$ ). In the shear force dominated case  $Ri \ll 1$ , the temperature variation is significant only very near to the walls, where the conductive heat transfer is dominant and in the middle portion of the cavity, temperature change is insignificant due to the recirculation of fluid, where the convective heat transfer is dominant. The bottom plots in the same **Figure 14** shows the case of different Grashof number ( $Gr = 10^6$ ). In this case the horizontal variation of temperature is more signifi-

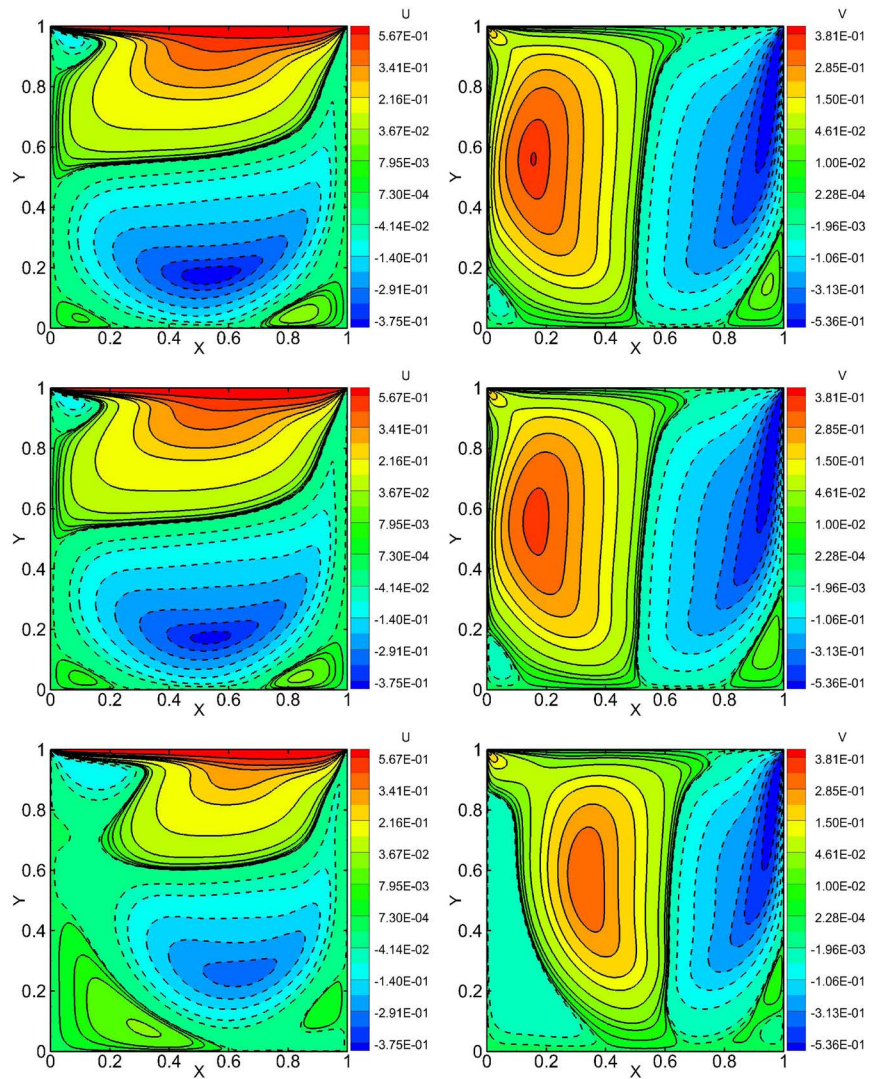


**Figure 11.** Contours of velocity components  $U$  (left) and  $V$  (right) for a fluid flow  $Re = 1000$  and  $Pr = 0.73$ . Here  $Ri = 0.01, 0.1$  and  $1$  respectively (top to bottom) or equivalently  $Gr = 10^4, 10^5$  and  $10^6$ . Here  $U$  is the horizontal component and  $V$  is the vertical component.

cant than the variation along the vertical direction. **Figure 15** shows the variation of temperature with  $Gr$  (top plot) and  $Pr$  (bottom plot) respectively. In this figure, the dash-dash line overlapping with the black continuous line which shows an insignificant change for the values of  $Gr = 10^4$  and  $Gr = 10^5$ . For  $Re = 1000$  it is observed that when  $Ri \leq 1$ , no significant changes in temperature takes place. However when  $Ri = 1$  the temperature along the vertical line of the cavity reduces considerably. For a fixed  $Re$  and  $Gr$ , for very low values of  $Pr$ , the temperature uniformly rises along the vertical distance and changes only slightly along the horizontal center of the cavity. However, if  $Pr \approx 1$  the temperature remains nearly constant in the middle of the cavity. For  $Pr \geq 1$ , a non-monotonic increase in  $T$  is noted, both along vertical and horizontal center region.

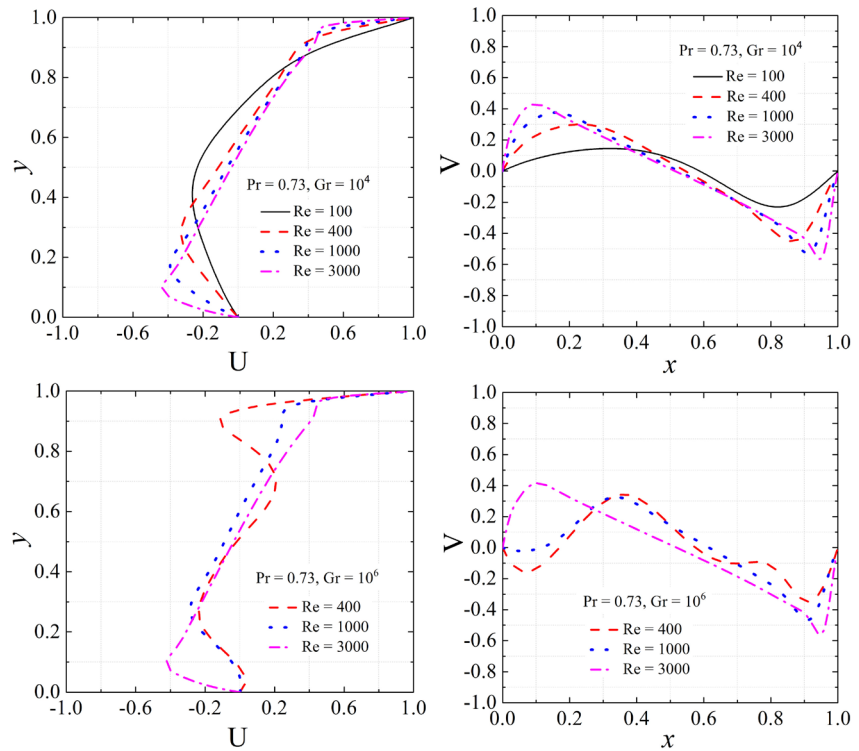


**Figure 12.** Horizontal and vertical components of velocity  $U$  and  $V$  along the center lines  $x = 0.5$  (left) and  $y = 0.5$  (right) are shown for  $Gr = 10^4$  (top) and  $Gr = 10^6$  (bottom) respectively. Here  $Pr = 0.73$ . Here, the dash-dot lines corresponding to  $Re = 3000$  are the forced convective cases.

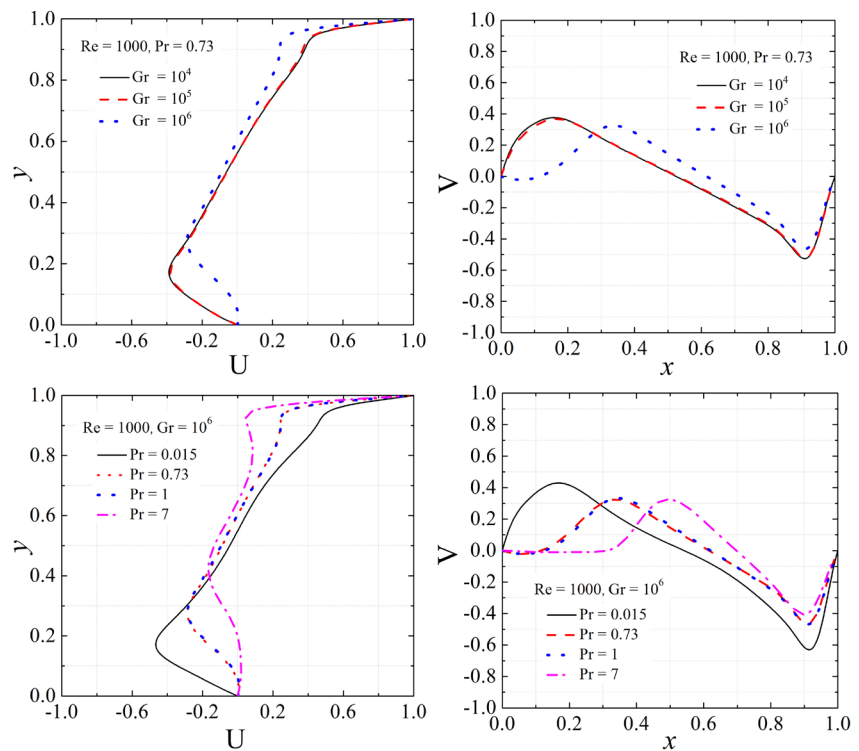


**Figure 13.** Profiles of horizontal velocity  $U$  along the vertical center line  $x = 0.5$  and vertical velocity  $V$  along horizontal center line  $y = 0.5$  are shown. Here  $Re = 1000$ .

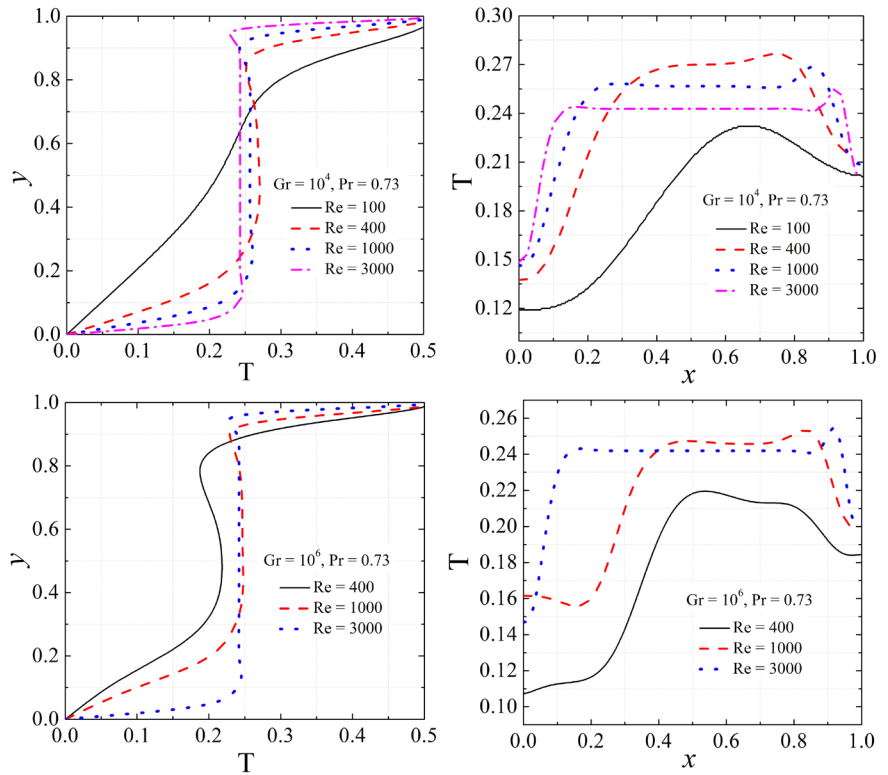


**Figure 14.** Temperature along the vertical center line  $x = 0.5$  (left) and along the horizontal center line  $y = 0.5$  (right) for  $Gr = 10^4$  and  $10^6$  respectively (top to bottom) are shown for  $Pr = 0.73$ .

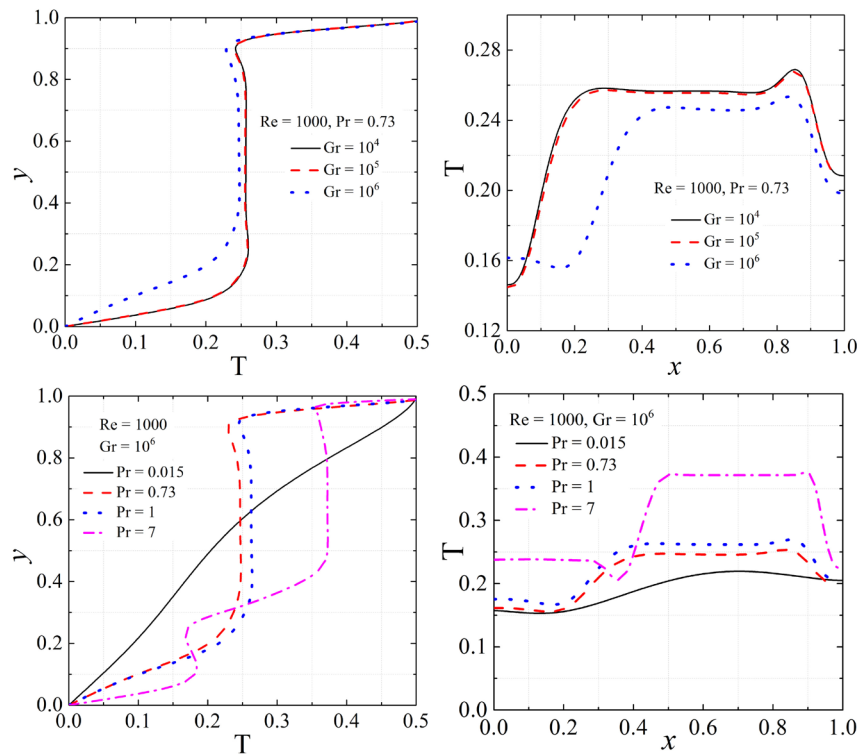


**Figure 15.** Temperature profiles along vertical and horizontal centers of the cavity for different  $Gr$  (top) and for different  $Pr$  (bottom).

### 6. Estimation of Order of Accuracy

We have checked the order of accuracy from the computed numerical values using the method of divided difference. In order to evaluate the accuracy of the obtained numerical results, we have taken the center point left corner (formed on the apex of vertical upstream wall and bottom surface) vortex ( $\psi_{\max}$ ) values for  $Re = 1000$ ,  $Pr = 0.73$  with all values of  $0 \leq Gr \leq 10^6$  having different grids of step size  $h$ . The reason for choosing the centre of vortex is the point where velocity of the fluid is nearly null ( $\psi$  is a constant), hence the singularity affected by the velocity vector due to corner vortices are avoided which is explained by Iwatsu *et al.*, [42]. The divided difference with respect to  $h$  is calculated as

$$\frac{\Delta(\phi)}{dh} = \frac{(\phi)_{h_1} - (\phi)_{h_2}}{h_1 - h_2} = y \tag{86}$$

A plot between  $y$  and the grid step size  $h$  is made on a log-log scale which is shown in **Figure 16**. The four points in the figure correspond to the values obtained in five different grids. It is found that result follow a straight line behaviour with a slope equal to 3. This is true for the flow with any  $Re, Pr$  and  $Gr$  considered in this study. Since the quantity in  $y$ -axis itself is equivalent to one slope, the overall slope should be 4, indicating that the numerical results obtained will be having fourth order accuracy.

### 7. Conclusion

The fourth order compact finite difference scheme is successfully implemented

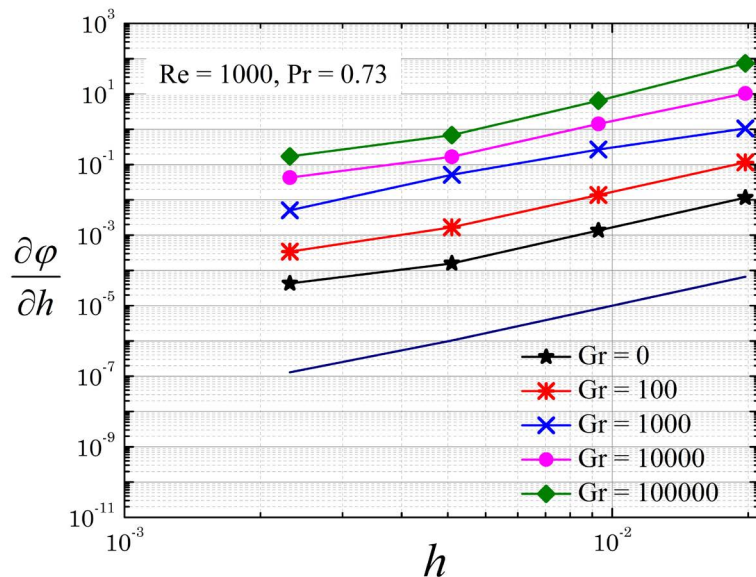


**Figure 16.** Log-log plot of divided differenced quantity  $d\phi/dh$  as a function of grid spacing  $h$ . Here  $\phi$  can be any physical quantity and we have taken it to be the  $\psi_{\max}$  for  $Re = 1000$  and  $Pr = 0.73$ . Plots connected with data points are computed from our discretization scheme. Bottom-most line is a line whose slope is equal to three.

To study the mixed convection in a lid driven cavity flow with linearly heated top wall. The multigrid iterative procedure allowed a fast convergence to the exact solution. The effect of heat transfer is affected by all the governing parameters as well as the effect of linear heating. The growth and the degradation of USE and DSE are observed for the increase of Richardson number, which shows a significant effect of  $Ri$  over heat transfer. In the mixed convection range, the USE and DSE are merging. The velocity contour shows that, both velocity components are responsible for the emergence of corner vortices. For  $Ri \geq 1$ , a push of buoyant force against the gravity occurs and hence the USE grows and finally it forms a separate cell near the bottom region of the cavity in the horizontal velocity component. The order of accuracy of the derived numerical scheme is found to be four.

### Acknowledgements

One of the authors (R. Sivakumar) would like to thank the UGC for supporting this research work through major project grant *vide* UGC project grant letter F. No. 37-312/2009 (SR) dated January 12, 2010, and also DST for infrastructure development funds through FIST program *vide* order SR/FST/PSII-021/2009 dated August 13, 2010. A. D. Abin. Rejeesh acknowledges the DST-INSPIRE fellowship *vide* DST/INSPIRE/Fellowship/2011/361 order dated August 01, 2013 and finally S. Udhayakumar acknowledges Pondicherry University for providing scholarship.

### References

- [1] Ghia, U. and Ghia, K.N. and Shin, C.T. (1982) High-Re Solution for Incompressible Flow Using the Navier-Stokes Equations and a Multigrid Method. *Journal of Computational Physics*, **48**, 13-15.
- [2] Cha, C.K. and Jaluria, Y. (1984) Recirculating Mixed Convection Flow for Energy Extraction. *International Journal of Heat and Mass Transfer*, **27**, 1801-1812.
- [3] Hsu, T.H. and Hsu, P.T. and How, S.P. (1997) Mixed Convection in a partially Divided Rectrangular Enclosure. *Numerical Heat Transfer, Part A: Applications*, **31**, 655-683. <https://doi.org/10.1080/10407789708914058>
- [4] Hsu, T.H. and Wang, S.G. (2000) Mixed Convection in a Rectrangular Enclosure with Discrete Heat Sources. *Numerical Heat Transfer, Part A: Applications*, **38**, 627-652. <https://doi.org/10.1080/104077800750021170>
- [5] Fedorov, A.G. and Visakanta, R. (2000) Three-Dimensional Conjugate Heat Transfer in the Microchannel Heat Sink for Electronic Packaging. *International Journal of Heat and Mass Transfer*, **43**, 399-415.
- [6] Leong, C.W. and Ottono, J.M. (1989) Experiments on Mixing Due to Chaotic Advection in a Cavity. *Journal of Fluid Mechanics*, **209**, 463-499. <https://doi.org/10.1017/S0022112089003186>
- [7] Alleborn, N. and Rasziller, H. (1999) Lid-Driven Cavity with Heat and Mass Transport. *International Journal of Heat and Mass Transfer*, **42**, 833-853.
- [8] Imberger, J. (1982) Dynamics of Lakes, Reservoirs and Cooling Ponds. *Annual Review of Fluid Mechanics*, **14**, 153-187. <https://doi.org/10.1146/annurev.fl.14.010182.001101>

- [9] Prasad, A.K. and Koseff, J.R. (1996) Combined Forced and Mixed Convection Heat Transfer in a Deep Lid-Driven Cavity Flow. *International Journal of Heat and Fluid Flow*, **17**, 460-467.
- [10] Elsherbiny, S.M. (1996) Free Convection in Inclined Air layers Heated from Above. *International Journal of Heat and Mass Transfer*, **39**, 3925-3930.
- [11] Prasad, Y.S. and Das, M.K. (2007) Hopt Bifurcation in Mixed Convection Flow inside a Rectangular Cavity. *International Journal of Heat and Mass Transfer*, **50**, 3583-3598.
- [12] Basak, T., Roy, S., Sharma, P.K. and Pop, I. (2009) Analysis of Mixed Convection Flows within a Square Cavity with Uniform and Non-Uniform Heating of Bottom Wall. *International Journal of Thermal Sciences*, **48**, 891-912.
- [13] Cheng, T.S. and Liu, W.H. (2010) Effect of Temperature Gradient Orientation on the Characteristics of Mixed Convection Flow in a Lid-Driven Square Cavity. *Computers and Fluids*, **39**, 965-978.
- [14] Erturk, E. and Gokol, C. (2006) Fourth Order Compact Formulation of Navier-Stokes Equations and Driven Cavity Flow at High Reynolds Numbers. *Numerical Methods in Fluids*, **50**, 421-436.
- [15] Cheng, T.S. (2011) Characteristics of Mixed Convection Heat Transfer in a Lid-Driven Square Cavity with Various Richardson and Prandtl Numbers. *International Journal of Thermal Sciences*, **50**, 197-205.
- [16] Ahmed, S.E., Oztop, H.F. and Al-Salem, K. (2016) Effects of Magnetic Field and Viscous Dissipation on Entropy Generation of Mixed Convection in Porous Lid-Driven Cavity with Corner Heater. *International Journal of Numerical Methods for Heat and Fluid Flow*, **26**, 1548-1566. <https://doi.org/10.1108/HFF-11-2014-0344>
- [17] Malleswaran, A. and Sivasankaran, S. (2016) A Numerical Simulation on MHD Mixed Convection in a Lid-Driven Cavity with Corner Heaters. *Journal of Applied Fluid Mechanics*, **9**, 311-319. <https://doi.org/10.18869/acadpub.jafm.68.224.22903>
- [18] Kareem, A.K., Gao, S. and Ahmed, A.Q. (2016) Unsteady Simulations of Mixed Convection Heat Transfer in a 3D Closed Lid-Driven Cavity. *International Journal of Heat and Mass Transfer*, **100**, 121-130.
- [19] Bettaibi, S., Sediki, E., Kuznik, F. and Succi, S. (2015) Lattice Boltzmann Simulation of Mixed Convection Heat Transfer in a Driven Cavity with Non-Uniform Heating of the Bottom Wall. *Communications in Theoretical Physics*, **63**, 91-100. <https://doi.org/10.1088/0253-6102/63/1/15>
- [20] Hussein, I.Y. and Ali, L.F. (2014) Mixed Convection in a Square Cavity Filled with Porous Medium with Bottom Wall Periodic Boundary Condition. *Journal of Engineering*, **20**, 99-119.
- [21] Ismael, M.A., Pop, I. and Chamkha, A.J. (2014) Mixed Convection in a Lid-Driven Cavity with Partial Slip. *International Journal of Thermal Sciences*, **82**, 47-61.
- [22] Mahapatra, T.R., Pal, D. and Mondal, S. (2013) Effects of Buoyancy Ratio on Double-Diffusive Natural Convection in a Lid-Driven Cavity. *International Journal of Heat and Mass Transfer*, **57**, 771-785.
- [23] Mekroussi, S., Nehari, D., Bouzit, M. and Chemloul, N.E.S. (2013) Analysis of Mixed Convection in an Inclined Lid-Driven Cavity with a Wavy Wall. *Journal of Mechanical Science and Technology*, **27**, 2181-2190. <https://doi.org/10.1007/s12206-013-0533-9>
- [24] Al-Salem, K., Oztop, H.F., Pop, I. and Varol, Y. (2012) Effects of Moving Lid Direction on MHD Mixed Convection in a Linearly Heated Cavity. *International Journal of Heat and Mass Transfer*, **55**, 1103-1112.

- [25] Basak, T., Pradeep, P.V.K., Roy, S. and Pop, I. (2011) Finite Element Based Heatline Approach to Study Mixed Convection in a Porous Square Cavity with Various Wall Thermal Boundary Conditions. *International Journal of Heat and Mass Transfer*, **54**, 1706-1727.
- [26] Mamourian, M., Shirvan, K.M. and Rahimi, R.E.A.B. (2016) Optimization of Mixed Convection Heat Transfer with Entropy Generation in a Wavy Surface Square Lid-Driven Cavity by means of Taguchi Approach. *International Journal of Heat and Mass Transfer*, **102**, 544-554.
- [27] Nayak, R.K., Bhattacharyya, S. and Pop, I. (2016) Numerical Study of Mixed Convection and Entropy Generation of Cu-Water Nanofluid in a Differentially Heated Skewed Enclosure. *International Journal of Heat and Mass Transfer*, **85**, 620-634.
- [28] Kefayati, G.H.R. (2015) FDLBM Simulation of Mixed Convection in a Lid-Driven Cavity Filled with Non-Newtonian Nanofluid in the Presence of Magnetic Field. *International Journal of Thermal Sciences*, **95**, 29-46.
- [29] Kefayati, G.H.R. (2014) Mixed Convection of Non-Newtonian Nanofluid in a Lid-Driven Enclosure with Sinusoidal Temperature Profile using FDLBM. *Powder Technology*, **256**, 268-281.
- [30] Jamai, H., Fakhreddine, S.O. and Sammouda, H. (2014) Numerical Study of Sinusoidal Temperature in Magneto-Convection. *Journal of Applied Fluid Mechanics*, **3**, 493-502.
- [31] Kefayati, G.H.R., Bandpy, M.G., Sajjadi, H. and Ganji, D.D. (2012) Lattice Boltzmann Simulation of MHD Mixed Convection in Lid-Driven Square Cavity with Linearly Heated Wall. *Scientia Iranica*, **19**, 1053-1065.
- [32] Arani, A.A.A., Sebdani, S.M., Mahmoodi, M., Ardeshiri, A. and Aliakbari, M. (2012) Numerical Study of Mixed Convection Flow in a Lid-Driven Cavity with Sinusoidal on Sidewalls Using Nanofluid. *Superlattices and Microstructures*, **51**, 893-911.
- [33] Nasrin, R. (2010) Mixed Magnetoconvection in a Lid-Driven Cavity with a Sinusoidal Wavy Wall and a Central Heat Conducting Body. *Journal of Naval Architecture and Marine Engineering*, **7**, 13-24. <https://doi.org/10.3329/jname.v8i1.6793>
- [34] Karimipour, A., Efse, M.H., Safaei, M.R., Semiromi, D.T., Jafari, S. and Kazi, S.N. (2014) Mixed Convection of Copper-Water Nanofluid in a Shallow Inclined Lid Driven Cavity Using the Lattice Boltzmann Method. *Physica A: Statistical Mechanics and Its Applications*, **402**, 150-168.
- [35] Chamkha, A.J. and Abu-Nada, E. (2012) Mixed Convection Flow in Single- and Double-Lid Driven Square Cavities Filled with Water- $\text{Al}_2\text{O}_3$  Nanofluid: Effect of Viscosity Models. *European Journal of Mechanics B-Fluids*, **36**, 82-96.
- [36] Garoosi, F. and Rashidi, M.M. (2015) Two Phase Simulation of Natural Convection and Mixed Convection of the Nanofluid in a Square Cavity. *Powder Technology*, **275**, 239-256.
- [37] Billah, M.M., Rahman, M.M., Sharif, U.M., Rahim, N.A., Sadidur, R. and Hasanuz-zaman, M. (2011) Numerical Analysis of Fluid Flow Due to Mixed Convection in a Lid-Driven Cavity Having a Heated Circular Hollow Cylinder. *International Communications in Heat and Mass Transfer*, **38**, 1093-1103.
- [38] Wesseling, P. (1982) Theoretical and Practical Aspects of a Multigrid Method. *SIAM Journal on Scientific and Statistical Computing*, **3**, 387-407. <https://doi.org/10.1137/0903025>
- [39] Zhang, J. (2003) Numerical Simulation of 2D Square Driven Cavity Using Fourth Order Compact Finite Difference Scheme. *Computers and Mathematics with Applications*, **45**, 43-52.

- [40] Botella, O. and Peyret, R. (1998) Benchmark Spectral Results on the Lid-Driven Cavity Flow. *Computers and Fluids*, **27**, 421-433.
- [41] Bruneau, C.H. and Saad, M. (1998) The 2D Lid-Driven Cavity Problem Revised. *Computers and Fluids*, **35**, 326-348.
- [42] Iwatsu, R., Hyun, J.M. and Kuwamura, K. (1993) Mixed Convection in a Driven Cavity with a Stable Vertical Temperature Gradient. *International Journal of Heat and Mass Transfer*, **36**, 1601-1608.
- [43] Sharif, M.A.R. (2007) Laminar Mixed Convection in Shallwl Inclined Driven Cavities with Hot Moving Lid on Top and Cooled from Bottom. *Applied Thermal Engineering*, **27**, 1036-1042.
- [44] Koseff, J.R. and Street, R.L. (1984) Visualization Studies of a Shear Driven Three-Dimensional Re-Circulating Flow. *Journal of Fluids Engineering*, **106**, 21-29. <https://doi.org/10.1115/1.3242393>
- [45] Koseff, J.R. and Street, R.L. (1984) The Lid-Driven Cavity Flow: A Synthesis of Qualitative and Quantitative Observations. *Journal of Fluids Engineering*, **106**, 390-398. <https://doi.org/10.1115/1.3243136>
- [46] Moallemi, M.K. and Jang, K.S. (1992) Prandtl Number Effects on Laminar Mixed Convection Heat Transfer in a Lid-Driven Cavity. *International Journal of Heat and Mass Transfer*, **35**, 1881-1892.
- [47] Torrance, K., Davis, R., Eike, K., Gill, P., Gutman, D., Hsui, A., Lyons, S. and Zien, H. (1972) Cavity Flows Driven by Buoyancy and Shear. *Journal of Fluid Mechanics*, **51**, 221-213. <https://doi.org/10.1017/S0022112072001181>
- [48] Schreiber, R. (1983) Driven Cavity Flows by Efficient Numerical Techniques. *Journal of Computational Physics*, **49**, 310-333.



Scientific Research Publishing

**Submit or recommend next manuscript to SCIRP and we will provide best service for you:**

Accepting pre-submission inquiries through Email, Facebook, LinkedIn, Twitter, etc.

A wide selection of journals (inclusive of 9 subjects, more than 200 journals)

Providing 24-hour high-quality service

User-friendly online submission system

Fair and swift peer-review system

Efficient typesetting and proofreading procedure

Display of the result of downloads and visits, as well as the number of cited articles

Maximum dissemination of your research work

Submit your manuscript at: <http://papersubmission.scirp.org/>

Or contact [ojfd@scirp.org](mailto:ojfd@scirp.org)

